https://doi.org/10.5194/acp-2020-1234
Preprint. Discussion started: 6 July 2021

Atmospheric Chemistry and Physics Discussions

Long-Term Atmospheric Emissions for the Coal Oil Point Natural Marine Hydrocarbon Seep Field, Offshore California

Ira Leifer[1], Christopher Melton[1], Donald R. Blake[2]

[1]Bubbleology Research International, Solvang, CA 93463, United States

[2]University of California, Irvine, Irvine, CA 92697, United States

Correspondence to: Ira Leifer (Ira.Leifer@bubbleology.com)

Abstract. In this study, we present a novel approach for assessing nearshore seepage atmospheric emissions through modeling of air quality station data, specifically, a Gaussian plume inversion model. Three decades of air quality station meteorology and total hydrocarbon concentration, *THC*, data were analysed to study emissions from the Coal Oil Point marine seep field offshore California. *THC* in the seep field directions was significantly elevated and Gaussian with respect to wind direction, θ. An inversion model of the seep field anomaly, $THC'(\theta)$, derived atmospheric emissions. The model inversion is for the far field, which was satisfied by gridding the sonar seepage and treating each grid cell as a separate Gaussian plume. This assumption was validated by offshore *in situ* offshore data that showed major seep area plumes were Gaussian. Plume air sample THC was 85% methane, CH_4, and 20% carbon dioxide, CO_2, similar to seabed composition, demonstrating efficient vertical plume transport of dissolved seep gases. Air samples also measured atmospheric alkane plume composition. The inversion model used observed winds and derived the three-decade-average (1990-2021) field-wide atmospheric emissions of 83,500±12,000 m^3 THC day^{-1}. Based on a 50:50 air to seawater partitioning, this implies seabed emissions of 167,000 m^3 THC dy^{-1}. Based on atmospheric plume composition, C_1-C_6 alkane emissions were 19, 1.3, 2.5, 2.2, 1.1, and 0.15 Gg yr^{-1}, respectively. The approach can be extended to derive emissions from other dispersed sources such as landfills, industrial sites, or terrestrial seepage if source locations are constrained spatially.

1 Introduction

1.1 Seepage and methane

On decadal timescales, the important greenhouse gas, methane, CH_4, affects atmospheric radiative balance far more strongly than carbon dioxide, CO_2 (IPCC, 2007, Fig. 2.21), yet CH_4 has large uncertainties for many sources (IPCC, 2013). Since pre-industrial times, CH_4 emissions have risen by a factor of ~2.5, and after stabilizing in the 1990s and early 2000s, resumed rapid growth since 2007 (Nisbet et al., 2019). The significantly shorter lifetime of CH_4 than CO_2 argues for CH_4 regulatory priority as emission reductions (and changes to the radiative balance) manifest more quickly as atmospheric concentrations decreases (Shindell, Faluvegi, Bell, & Schmidt, 2005). Further impetus for a CH_4 focus is a recent estimate that 40% CH_4 emissions reductions are feasible at no net cost for the oil and gas, O&G, industry (IEA, 2020), a major anthropogenic CH_4 source (IPCC, 2014). This is particularly salient given recent estimate that recent CH_4 increases are half from the O&G industry (Jackson et al., 2020).

https://doi.org/10.5194/acp-2020-1234
Preprint. Discussion started: 6 July 2021

Atmospheric Chemistry and Physics Discussions

For 2008-2017, global CH_4 top-down emissions estimates are 576 Tg yr^{-1}; 1 Tg=10^{12} g, (550-594 Tg yr^{-1}) whereas bottom-up approaches find 737 Tg yr^{-1} (594-881 Tg yr^{-1}). Anthropogenic sources for 2008-2017 are estimated at 336-376 Tg CH_4 yr^{-1} based on bottom-up estimates. Natural sources include wildfires, wetlands, hydrates, and geological seepage among others. Bottom-up estimates for natural sources are higher than top-down estimates including for geological sources (Saunois et al., 2020). Geological sources (including seepage) are estimated at 63-80 Tg CH_4 yr^{-1} with marine seepage estimated to contribute 20-30 Tg CH_4 yr^{-1} (Etiope, Ciotoli, Schwietzke, & Schoell, 2019) or 5-10 Tg CH_4 yr^{-1} (Saunois et al., 2020). For comparison, marine non-geological CH_4 emissions are estimated at 4-10 Tg yr^{-1}. The divergence of seepage emissions is based on uncertainty in the fraction of seabed emissions that reaches the atmosphere and uncertainty in overall seabed emissions. Further complexity in assessing geological seepage CH_4 emissions arise because both seepage and O&G emissions source from the same geological reservoirs (Leifer, 2019) and thus are isotopically similar (Schwietzke et al., 2016).

Seepage is where the migration of petroleum hydrocarbon gases and fluids in the lithosphere escape to the hydrosphere and/or atmosphere from the reservoir formation where they have accumulated. The reservoir is sealed by a capping layer to allow hydrocarbon accumulation. Thus, seepage requires a migration pathway through the capping layer (Abrams, 2005), or the capping layer has been eroded away leaving a reservoir formation outcropping.

Marine seepage is widespread in every sea and ocean (Judd & Hovland, 2007). Quantitative seepage estimates (for global budgets) are limited (though growing); see Leifer (2019) review and below for more recent. Fluxes for individual marine seep vents and seep areas have been reported for the Gulf of Mexico (Johansen et al., 2020; Leifer & MacDonald, 2003; Römer et al., 2019; T. C. Weber et al., 2014), the Black Sea (Greinert, McGinnis, Naudts, Linke, & De Batist, 2010), the southern Baltic Sea (Heyer & Berger, 2000), various sectors of the North Sea (Borges, Champenois, Gypens, Delille, & Harlay, 2016; Leifer, 2015; Römer et al., 2017), offshore Norway (Muyakshin & Sauter, 2010; Sauter et al., 2006) and offshore Svalbard in the Norwegian Arctic (Veloso-Alarcón et al., 2019), offshore Pakistan (Römer, Sahling, Pape, Bohrmann, & Spieß, 2012), the arctic Laptev Sea (Leifer, Chernykh, Shakhova, & Semiletov, 2017), the East Siberian Arctic Sea (Shakhova et al., 2013), the South China Sea (Di, Feng, Tao, & Chen, 2020), New Zealand's Hikurangi Margin (Higgs et al., 2019), the Cascadia Margin (Riedel et al., 2018), and the Coal Oil Point (COP) marine hydrocarbon seep field, hereafter COP seep field, in the northern Santa Barbara Channel, offshore Southern California (Hornafius, Quigley, & Luyendyk, 1999), and for numerous individual vents in the field (Leifer, 2010).

Most seep emission estimates are from short-term field campaigns that provide a snapshot rather than annualized values. Seep emissions vary on timescales from tidal (Leifer & Boles, 2005; Römer, Riedel, Scherwath, Heesemann, & Spence, 2016) to seasonal (Bradley, Leifer, & Roberts, 2010) to decadal (Fischer, 1978; Leifer, 2019). Additional temporal variability arises from transient emissions – pulses lasting seconds to minutes (Greinert, 2008; Schmale et al., 2015) to decades (Leifer, 2019). This shortcoming is being addressed by benthic (seabed) observatories and cabled

https://doi.org/10.5194/acp-2020-1234
Preprint. Discussion started: 6 July 2021

Atmospheric Chemistry and Physics Discussions

observatories, e.g., Wiggins, Leifer, Linke, and Hildebrand (2015); Greinert (2008), (Kasaya et al., 2009; Römer et al., 2016; Scherwath et al., 2019). Still, benthic observatories are costly and thus rare.

Seepage contributes to oceanographic budgets and to a lesser extent, atmospheric budgets due to water column losses with significant uncertainty in the partitioning. As a result, uncertainty in the atmospheric contribution is much larger than the (significant) uncertainty in seabed emissions. Seepage partitioning between the atmosphere and ocean - where microbial degradation occurs on timescales inversely related to concentration (Reeburgh et al., 1991) - depends primarily on depth (Leifer & Patro, 2002), with little to none of deepsea seabed emissions reaching the atmosphere, e.g., (Römer et al., 2019). In contrast, very shallow seepage (meter scale) largely entirely reaches the atmosphere by both direct bubble-meditated transfer and diffusive transport. For intermediate depths, the ocean/atmospheric partitioning is complex and depends on depth, bubble flux, bubble size distribution, and bubble surface conditions, among other characteristics (Leifer & Patro, 2002), whereas the indirect diffusive flux (proximate and distal) depends on bubble dissolution depth (Leifer & Patro, 2002), turbulence vertical transport in the winter wave-mixed layer (Rehder, Keir, Suess, & Rhein, 1999), microbial oxidation losses, and exchange through the sea-air interface.

A range of approaches have been used to estimate the sea-air flux. The most common is by measuring the atmospheric and water concentrations and applying air-sea gas exchange theory for the measured wind speeds, e.g., Schmale, Greinert, and Rehder (2005) for Black Sea seepage under weak wind speeds.

Sea-air exchange is a diffusive turbulence transfer process that depends on the air-sea concentration difference and the piston velocity, k_T, which depends on gas physical properties, wind speed, u (Liss & Duce, 2005), wave development (Zhao, Toba, Suzuki, & Komori, 2003), wave breaking (Liss & Merlivat, 1986), and surfactant layers at low wind speeds which suppress gas exchange (Frew et al., 2004). k_T increases rapidly and non-linearly with u and has been parameterized as piecewise linear functions (Wanninkhof, Asher, Ho, Sweeney, & McGillis, 2009) or as a cubic function (Nightingale et al., 2000). Air-sea gas exchange theory is for (relatively) homogeneous atmospheric and oceanographic fields (concentrations, winds, wave development), and thus is inappropriate for point-source (bubble-plume) emissions and for the near-field downcurrent plume, which tends to be heterogeneous.

An alternate approach is to derive atmospheric emissions by Gaussian plume inversion. Leifer, Luyendyk, Boles, and Clark (2006) derived emissions for a blowout from Shane Seep in the COP seep field. This neglects of course, the portion that dissolves in the ocean and drifts downcurrent out of the bubble plume's vicinity – the dissolved portion that evades the ocean in the vicinity of the plume is counted by the inversion. Finally, seabed bubble size measurements or an assumed bubble size distribution can be used to initialize a numerical bubble model to predict atmospheric direct fluxes (Leifer et al., 2017; Schneider von Deimling et al., 2011). Additionally, a dispersive model for the fraction of bubble-mediated transported gases to the wave mixed layer could then estimate the indirect diffusive atmospheric emissions by turbulence transport and sea-air gas evasion. As noted, there are many variables, many of which may not be measured, emphasizing the importance of model validation.

https://doi.org/10.5194/acp-2020-1234
Preprint. Discussion started: 6 July 2021

Atmospheric Chemistry and Physics Discussions

108

109 **1.2 Study motivation**

110 In this study, we present a novel approach for assessing nearshore seepage atmospheric emissions –air quality station
111 data modeling, specifically using a Gaussian plume inversion model. This model requires that source locations are
112 mapped, spatially stable, and lie within a fairly constrained distance range band. These conditions are met for the West
113 Campus air quality Station (WCS) and the nearby offshore Coal Oil Point (COP) marine hydrocarbon seep field. COP
114 seep field lies in shallow coastal waters of northern Santa Barbara Channel, CA. Spatial constraint is provided by
115 geological structures, such as faults, that constrain emission locations. The Gaussian plume model assumes the source
116 is in the far field, whereas WCS is in the nearfield for the extensive COP seep field. To satisfy the far field criterion,
117 the source was gridded and each grid cell's emissions treated as a distinct (distant) Gaussian plume. This
118 characterization was validated in an offshore survey of several focused COP seep field seepage areas, which were
119 well-modeled as Gaussian plumes.
120
121 Thus, this study demonstrates a novel approach to deriving emissions from an air quality station data for an area source
122 such as natural marine seepage. This approach could be used to derive emissions from other dispersed sources such
123 as landfills, industrial sites, or natural terrestrial seepage where the source locations can be constrained spatially.
124

125 **1.3 Water column marine seabed seepage fate**

126 Seep seabed CH_4 partitions between the atmosphere and water column depends on seabed depth and emission
127 character – as bubbles, bubble plumes (Leifer & Patro, 2002), or dissolved CH_4. Dissolved CH_4 migration through the
128 sediment is oxidized largely by near seabed microbes (Reeburgh, 2007), termed the microbial filter, negating its
129 contribution. Thus, CH_4 transport through the seabed's microbial filter is bubble-mediated.
130
131 As seep bubbles rise, they dissolve, losing gas to the surrounding water at a rate that decreases with time; smaller and
132 more soluble gases dissolve faster than larger and less soluble gases, i.e., fractionation (Leifer & Patro, 2002).
133 Additionally, larger bubbles transport their contents upwards more efficiently than smaller bubbles (Leifer et al.,
134 2006). Sufficiently large bubbles reach the sea surface with a significant fraction of their seabed CH_4 from depths of
135 even hundreds of meters (Solomon, Kastner, MacDonald, & Leifer, 2009). There are synergies, too with higher plume
136 fluxes driving a stronger upwelling flow that transports plume fluids with dissolved gases upwards towards the surface
137 where air-sea gas exchange drives evasion (Leifer, Jeuthe, Gjøsund, & Johansen, 2009). Another synergy is from
138 elevated dissolved plume CH_4 concentration (Leifer, 2010; Leifer et al., 2006), which slows dissolution. Also, bubbles
139 are oil-coated, which slows dissolution.
140
141 Moreover, gases in bubbles that dissolve in the wave mixed layer (or reaches it by the upwelling flow), then diffuse
142 by turbulence to the air-sea interface. Note, some of this dissolved CH_4 is removed by microbial degradation and thus

https://doi.org/10.5194/acp-2020-1234
Preprint. Discussion started: 6 July 2021

Atmospheric Chemistry and Physics Discussions

never reaches the air-sea interface. Thus, there are two timescales that govern the fraction that evades – the microbial degradation timescale, which decreases as concentrations increase, and the diffusion timescale, which decreases with increasing wind speed. As a result, there is a dissolved plume that drifts downcurrent, from which evasion creates a linear-source atmospheric plume, with dissolved plume concentrations decreasing with time from sea-air gas exchange losses, microbial oxidation, and diffusion.

1.4 Atmospheric Gaussian plumes

Strong focused atmospheric plumes are created from seep bubble bursting at the sea surface and dissolved gas evasion within the bubble surfacing footprint, which is enhanced by water-side turbulence from rising and bursting bubbles (Leifer et al., 2015). The atmospheric plume evolution is described by the Gaussian plume model (Hanna, Briggs, & Hosker Jr., 1982), which relates downwind concentrations to wind transport and turbulence dispersion and is described in **Supp. Sec. S1**.

1.5 Setting

1.5.1 The Coal Oil Point seep field

The COP seep field (**Fig. 1**) is one of the largest seep fields in the world, with estimated seabed emissions, E_B, for 1995-1996 of $1.5x10^5 \pm 2x10^4$ m^3 THC dy^{-1} (Hornafius et al., 1999). Hereafter emissions and concentrations are for total hydrocarbon, THC, unless noted. Of these seabed emissions, Clark, Washburn, Hornafius, and Luyendyk (2000) estimated that half the COP seep field E_B reach the atmosphere in the near field. This is due to shallowness, bubble oiliness, high plume bubble densities, and turbulence mixing within the wave mixed layer.

Geological structures play a critical role in the spatial distribution of seepage (Leifer, Kamerling, Luyendyk, & Wilson, 2010), which lies along several trends in waters from a few meters to ~85 m deep. These trends follow geologic structures including anticlines, synclines, and faults in the reservoir formation, the Monterey Formation. Faults provide migration pathways with seepage scattered non-uniformly along the trends, including focused seep areas that are highly active, localized, and often are associated with crossing faults and fractures (Leifer et al., 2010). Seepage in these areas typically surrounds a focus and decreases with distance, primarily along linear trends (Leifer, Boles, Luyendyk, & Clark, 2004). See **Supp. Table S3** for informal names and locations of selected focused seep areas.

1.5.2 Coal Oil Point seep field emissions and composition

COP seep field sources from the South Ellwood oil field whose primary source rock is Monterey Formation, which is immature to marginally mature. Petroleum gases from marine organic materials have relatively higher proportion of ethane, propane, butane, etc., relative to methane as compared to petroleum gases from terrestrial organic materials. The wet gas fraction (C_2-C_5/C_1-C_5) indicates a thermogenic origin of greater than 0.05 (Abrams, 2017). Of the

https://doi.org/10.5194/acp-2020-1234
Preprint. Discussion started: 6 July 2021

Atmospheric Chemistry and Physics Discussions

177 saturated alkanes, the alkenes (olefins) are of biological origin. Additionally, the ethane/ethene ratio and
178 propane/propene ratios can be indicators of seep gas biogenic modification with values above 1000 indicating purely
179 thermogenic origin (Abrams, 2017; Bernard, Brooks, & Zumberge, 2001).
180
181 In this study, we analyse WCS (located at 34° 24.897'N, 119° 52.770'W) atmospheric THC. Clark, Washburn, and
182 Schwager (2010) report average seep field seabed CH_4, CO_2, and non-methane hydrocarbons (NMHC), of 76.7, 15.3,
183 and 7.7%, respectively, with Trilogy Seep seabed compositions of 67, 21, and 7.8%, respectively. With respect to
184 alkanes, seabed bubbles are 90.4% CH_4 and 8.6% NMHC. CO_2 rapidly escapes the bubbles and is negligible (<1%)
185 at the sea surface. At the sea surface, CH_4 in bubbles is ~90% with NMHC making up the remaining 10%, neglecting
186 air gases (Clark et al., 2010). Note, whereas seep THC is predominantly CH_4, THC from terrestrial directions arises
187 from NMHC from traffic and other anthropogenic sources as well as CH_4 from pipeline leaks, terrestrial seeps, etc.
188

189 **1.5.3 Northern Santa Barbara Channel climate**

190 Diurnal and seasonal wind cycles are important to the transport of the seep atmospheric emissions. The Santa Barbara
191 climate is Mediterranean with a dry season and a wet seasons when storms occur infrequently (Dorman & Winant,
192 2000). The semi-permanent eastern Pacific high-pressure system plays a dominant controlling role in weather in the
193 Santa Barbara coastal plain. This high-pressure system drives light winds and strong temperature inversions that act
194 as a lid that restricts convective mixing to lower altitudes. The coastal California boundary layer is shallow, 0 to 800
195 m (Edinger, 1959), generally 240-300 m around Santa Barbara (Dorman & Winant, 2000). Additionally, coastal
196 mountains provide physical barriers to transport (Lu, Turco, & Jacobson, 1997).
197
198 As a coastal environment, the land/sea breeze is important to overall wind flow patterns with weak offshore night
199 winds and stronger onshore afternoon winds (Dorman & Winant, 2000). In coastal Santa Barbara, warming on
200 mountaintops and more interior arid land relative to cooler marine temperatures drives the sea breeze. Downslope
201 nocturnal flows warm nighttime surface temperatures, moderating the coastal diurnal temperature cycle (Hughes, Hall,
202 & Fovell, 2007).
203
204 Typical morning winds are calm and offshore, often accompanied by a cloud-filled marine boundary layer, just 50–
205 150 m thick (Lu et al., 1997). The marine layer usually (but not always) "burns off" mid–morning after which
206 temperatures rise, the boundary layer thickens and winds shift clockwise from offshore to eventually prevailing
207 westerlies aligned with the coastal mountains. Mid-day through the afternoon, winds strengthen, often leading to
208 whitecapping that can continue into the evening before the boundary layer collapses and winds return to the nocturnal
209 pattern.
210

https://doi.org/10.5194/acp-2020-1234
Preprint. Discussion started: 6 July 2021

Atmospheric Chemistry and Physics Discussions

2 Methods

2.1 West Campus Station data

WCS data includes wind speed, u, direction, θ, and THC concentration, C. Daily instrument calibration occurs after midnight, rendering C unavailable 00:50 to 02:09 local time, LT. WCS was improved significantly in 2008 from 1-hour to 1-minute time resolution, which allowed far higher values of C and u due to the shorter averaging times. Data analysis uses custom routines as well as standard routines and functions in MATLAB (MathWorks, MA).

First, WCS data were quality controlled to remove all values of C during the daily calibration, as well as to interpolate neighboring values that were unrealistically low, i.e., C less than 1.6 ppm in the 1990s and 1.85 ppm in the 2000s. Data since 2008 were smoothed by nearest-neighbor averaging, yielding 3-minute time resolution. Data prior to 2008 were hourly and were not smoothed. Wind data were nearest-neighbor averaged after decomposing into north and east components, followed by recalculation of u and θ.

2.2 *In situ* marine surveys

Offshore *in situ* survey data were collected by the *F/V Double Bogey*, a 12-m, 9-ton, fishing vessel with a near waterline deck (~0.2 m) and low overall profile (cabin at ~2.2 m). A sonic anemometer (VMT700, Vaisala) was mounted on a 6.5 m, 5-cm (2") diameter aluminum mast and measured 3D winds. Continuous, 5 Hz CH_4 and CO_2 data were collected by a Cavity Enhanced Absorption Spectroscopy (CEAS) analyzer (FGGA, LGR Inc., San Jose, CA). Vessel location and time were from a Global Positioning System (GPS) at 1 Hz (19VX HVS, Garmin, KS). CH_4 and CO_2 calibration with a greenhouse gas air calibration standard (CH_4: 1.981 ppmv; CO_2: 404 ppmv, Scott Marin, CA, purchased 2015, Sigma Aldritch, St Louis, MO).

Data are real time integrated and visualized in Google Earth on a portable computer (Spectre360, HP) using custom software, written in MATLAB (MathWorks, MA) for AutoMObile trace Gas (AMOG) Surveyor, described elsewhere (Leifer, Melton, Fischer, et al., 2018; Leifer, Melton, Manish, & Leen, 2014; Leifer, Melton, Tratt, et al., 2018; Leifer et al., 2016). Real-time visualization facilitates adaptive surveys, wherein the survey route is modified based on real time data to improve outcomes (Thompson et al., 2015) - in this case to facilitate plume tracking and to ensure transects were near orthogonal to the wind.

Accurate, absolute winds are calculated from relative winds after accounting for vessel motion and filtering for non-physical velocity changes due to GPS uncertainty (Leifer, Melton, Fischer, et al., 2018). Filtering removes transient wind speeds that are not relevant to plume transport. The filter interpolates GPS positions flagged as unrealistic.

Whole air samples were collected in evacuated 2-liter stainless steel canisters, which were filled gently over ~1 minute from ~1 m above the sea surface. The filled canisters were analyzed in the Rowland/Blake laboratory at the University

https://doi.org/10.5194/acp-2020-1234
Preprint. Discussion started: 6 July 2021

Atmospheric Chemistry and Physics Discussions

of California, Irvine for carbon monoxide, CO, CH_4, and C_2-C_7 organic compounds. Samples were analysed by a gas chromatography multi-column/detector analytical system utilizing flame ionization detection.

2.3 Seep plume emissions model

The plume inversion model is a three-step process (Leifer, Melton, Fischer, et al., 2018; Leifer, Melton, Tratt, et al., 2018; Leifer et al., 2016). Emissions from focused seep areas were derived from offshore data by first fitting Gaussian function(s) to orthogonal transect *C'* data, termed the data model. *C'* is relative to *C* outside the plume, derived by linear interpolation across the plume. The data model is derived by error minimization using a least-squares linear-regression analysis (Curve fitting toolbox, MathWorks, MA). Next, the Gaussian plume model (**Eqn. S1; Supp. Figs. S1; S2**) is fit to the data model. Transect data are collected close to orthogonal to the wind direction and are projected in the wind direction onto an orthogonal plane. A validation study of the approach is described in Leifer, Melton, Tratt, et al. (2018) where model-derived emissions were compared with remote sensing-derived emissions (which are largely insensitive to transport). The study found *in situ* and remote-sensing derived emissions agreed within 11%.

2.4 Seep field emissions model

The seep plume emissions inversion model is based on gridding the seep field into numerous small additive Gaussian plumes to represent the area emissions and was written in MATLAB (MathWorks, MA). This assumes that each sea-surface grid cell contributes a Gaussian plume, an assumption that was tested with offshore survey data downwind of several active seep areas.

The definition of area versus point source depends on the relevant length scales – an area source is well approximated as a point-source plume if sufficiently downwind (far field), where the downwind distance depends on the source's size scale and meteorological conditions. Whereas WCS is near field for the entire seep field plume, the small plumes from each grid cell is in the far field for WCS.

The area source was based on a Sept. 2005 sonar survey sonar return, ω, map (**Fig. 1**), see Leifer et al. (2010) for sonar survey details. Simulations used sonar data gridded at a hybrid 22/56-m in a UTM coordinate system, with origin at WCS. Specifically, gaps in the 22-m map were filled from the 56-m map (**Supp. Fig. S3**). The probability distribution of ω was used to identify the noise level (**Supp. Fig. S4**) as in Leifer et al. (2010).

The model calculates a Gaussian plume for $E(i,j)$ for grid cells *i00* and *j*, for each grid cell with ω above noise for the observed $u(\theta)$ in the wind direction θ and a typical Santa Barbara channel boundary layer. The initial $E(i,j)$ is by scaling such that the integrated sonar return ($\int\omega(x,y)$) scales to E=1.5x10^5 m^3 dy^{-1}, i.e., E_B from Hornafius et al. (1999). The Gaussian plume is calculated in a Cartesian coordinate system (**Supp. Fig. S5A**) and then rotated to θ and linearly interpolated to double the spatial resolution. The rotated plume then is regridded to UTM coordinates using the

https://doi.org/10.5194/acp-2020-1234
Preprint. Discussion started: 6 July 2021

Atmospheric Chemistry and Physics Discussions

ffgrid.m function (**Supp. Fig. S5B**). Interpolation helps prevent gaps in the regridded plume map. The regridded plume is renormalized to ensure total mass is conserved before and after these operations. Rotated plumes are translated to the seep field grid and added, yielding $C'_{Sim}(i,j)$, the simulated plume anomaly (**Supp. Fig. S5C**).

The model scans θ for the seep directions (110°<θ<330°) and calculates the simulated plume anomaly, $C'_{Sim}(\theta)$ at WCS, which is compared with the observed $C'_{Obs}(\theta)$ at WCS. Hereafter, C_{Obs} and C_{Sim} and their anomaly refer to values at WCS. $C'_{Obs}(\theta)$ is defined:

$$C'_{Obs}(\theta) = C_{Obs}(\theta)\text{-min}(C_{Obs}(\theta)) \quad (1)$$

with the minimum typically from the west. Specifically, $C'_{Obs}(\theta)$ was calculated by subtracting the minimum in the annualized observed $C'_{Obs}(t,\theta)$ each year, t, after applying a 7-year running average.

Emissions from suburban communities, light industry, and commercial centers enhance $C'_{Obs}(\theta)$ for the north to east (~350-70°) sectors. Removal of these terrestrial emissions was by fitting a Gaussian function to $C'_{Obs}(\theta)$ for 330°<θ<30° with the residual yielding $C'_{Obs}(\theta)$. This only affected $C'_{Obs}(\theta)$ for directions corresponding to the fields' eastern edge.

Simulations were run at angular resolutions of 2°. Higher angular resolution produced small-scale artifacts for the 22/56-m sonar grid while the 11-m sonar grid was overly sparse due to the distance between sonar tracks (**Supp. Fig. S3**).

The modeled source is from ω (in decibels), whereas emissions are moles m^{-2} s^{-2}. Given that the relationship between ω and bubble density (emissions) is complex and non-linear (Leifer et al., 2017), there is poor agreement between $C'_{Sim}(\theta)$ and $C'_{Obs}(\theta)$. Thus, a correction function, $K(\theta)$, is applied to emissions for each grid, $E(i,j)$, along each θ and the model rerun. $K(\theta)$ is:

$$K(\theta) = {C'_{Obs}(\theta)}/{C'_{Sim}(\theta)}. \quad (2)$$

Initially, K=1, but in subsequent iterations, $K(\theta)$ is scaled as in **Eqn. 2** to adjust E in cells along θ. Because $K(\theta)$ weights closer seeps more than more distant seeps, a normalized distance varying correction function, $K(r,\theta)$, was calculated such that,

$$\int_{r=0}^{r=\infty} E(r,\theta) = \int_{r=0}^{r=\infty} K(r,\theta)\, E(r,\theta)\, dr \quad (3)$$

where r is distance from WCS. Simulations that shifted WCS northwards showed E was varying nearly linearly. Accounting for off-axis plume contributions requires several iterations to achieve *Convergence* defined,

$$Convergence = {\sum C'_{Sim}(\theta)\ \sum C'_{Obs}(\theta)}/{\sum C'_{Obs}(\theta)} \quad (4)$$

https://doi.org/10.5194/acp-2020-1234
Preprint. Discussion started: 6 July 2021

Atmospheric Chemistry and Physics Discussions

313 Iterations were stopped after achieving *Convergence* of 1% or better – typically 4 to 5 iterations. Simulations suggested
314 wind veering, ψ, was important, which was implemented by calculating Gaussian plumes for θ and assigning it to
315 $C'(\theta + \psi)$.
316

317 **3 Results**

318 **3.1 Offshore *in situ* surveys**

319 An offshore COP seep field survey measured *in situ* C_{CH4} and u on 28 May 2016. Data were collected from the Santa
320 Barbara harbor (~7.5 km east of the seep field, **Fig. 2A; Supp. Fig. S6**) to offshore Naples, several kilometers west
321 of the seep field. Winds were fairly consistent easterlies over most of the seep field. Winds had an onshore component
322 near Campus Point and a broad (6-km wide) offshore flow west of COP that shifts to along coast near Naples (**Fig.**
323 **2A, white arrows**). Observed winds veered ~10° from east to the west sides of the seep field, roughly comparable to
324 the shift in coastline orientation.
325
326 Plumes are apparent downwind of major seeps, with the largest associated with the Trilogy Seep (**Fig 2B**). Strong
327 plumes also are evident downwind of the La Goleta Seep and Patch Seep. Notably, the Seep Tent Seep plume was
328 very weak. The Seep Tent Seep was the dominant seep area in the COP seep field from its appearance in June 1973
329 (Boles, Clark, Leifer, & Washburn, 2001) until recent years.
330
331 Additionally, the offshore survey identified focused plumes from beyond the extent of the seep field's 2005-sonar
332 map. Specifically in the Goleta Bay, which has been noted (Jordan et al., 2020), and offshore Haskell and Sands
333 Beaches, areas of abandoned oil wells.
334
335 Plume alkane *C'* were determined by the difference between two "background" air samples collected immediately
336 outside the plume and three Trilogy Seep plume air samples. CH_4 was 88.5% of THC, with ethane, propane, and
337 butane at 3.1%, 4.2%, and 2.76%, respectively, with pentane, hexane, and heptane at 1.11, 0.13, and 0.04%,
338 respectively (**Table 1**). THC molecular weight is 19.6 g $mole^{-1}$ based on a composition weighting. Branched alkanes
339 were detected, with 2-methylpentane and 3-methylpentane comprising 0.21%, each, as well as simple aromatics, e.g.,
340 benzene and toluene, with concentrations of 0.044 and 0.100 ppm, respectively.
341
342 The observed wet gas fraction (C_2-C_5/C_1-C_5) was 0.11 indicating a thermogenic origin (greater than 0.05 (Abrams,
343 2017)) and derivation from marine organic materials. Although the olefins ethene and ethyne were detectable at 0.02%
344 and 0.004%, respectively, butene was not detected. These olefins primarily derive from microbial processes (Abrams,
345 2017), thus, the ethane/ethyne ratio of 6200 also strongly indicates a thermogenic source (Bernard et al., 2001).
346 Atmospheric CO_2 was elevated by 12 ppm. Given that CO_2 completely dissolves from bubbles well before reaching
347 the sea surface (Clark et al., 2010), this demonstrates vertical transport of enhanced dissolved gases to the sea surface.

https://doi.org/10.5194/acp-2020-1234
Preprint. Discussion started: 6 July 2021

Atmospheric Chemistry and Physics Discussions

348

349 Plumes for the Trilogy Seeps, La Goleta Seep, and Seep Tent Seep were inverse modeled to derive emissions using
350 the average winds across each plume. For the Trilogy Seeps, u was 5.9 m s^{-1}, insolation full sun, and the source height
351 was 25 m based on Trilogy's atmospheric plume being buoyant. Model surface concentrations for Trilogy B plume
352 are shown in **Fig 2A**. The other two seeps are far less intense and used a 1-m source height.

353

354 E for Trilogy A was 1.28 Gg CH_4 yr^{-1} (5600 m^3 CH_4 dy^{-1}), whereas Trilogy B and C contributed 0.06 and 0.07 Gg
355 CH_4 yr^{-1}, respectively, for a total of 6200 CH_4 m^3 dy^{-1}. Note, the plume origins and the sonar locations do not precisely
356 match because bubble surfacing location / atmospheric plume source are deflected by currents from the sonar-mapped
357 seabed vent location. Deflections can be up to ~40 m. La Goleta Seep released 4000 m^3 CH_4 dy^{-1} and the Seep Tent
358 Seep released 310 m^3 CH_4 day^{-1} with almost no surface bubble expression. For comparison, Clark et al. (2010) used a
359 flux buoy, which measures near surface bubble fluxes, and found Trilogy Seep emissions of 5500 and 4200 m^3 THC
360 dy^{-1} and 930 m^3 THC day^{-1} for La Goleta Seep in 2005 and 5700 m^3 THC dy^{-1} for the Seep Tent Seep in 2002. During
361 the cruise, surface bubble plumes were not observed for the Seep Tent Seep, although its bubble plume had been a
362 perennial and dominant feature since its appearance. Note, Clark et al. (2010) reported THC in near sea surface bubbles
363 was 91% CH_4.

364

365 **3.2 West Campus Station**

366 **3.2.1 Temporal trends**

367 WCS is 500 m from the coast (to the southwest) at 11-m altitude and 850 m almost due south to the 11-m altitude
368 bluffs of Coal Oil Point (**Fig. 1**). Terrain slopes gently towards the coast to the southwest and towards a lagoon to the
369 south-southeast, rising again to the southeast to the COP bluffs. This flat relief likely has small to negligible effect on
370 wind speed and direction, although differential land-ocean heating could influence winds. Wind veering for the coast
371 to the east of COP is likely due to the orientation of the coastline and bluffs.

372

373 The WCS improvements in 2008 (**Fig. 3-dashed line**) allowed far higher values of C and u (**Supp. Fig. S7A,7B**).
374 Comparison of the probability distributions of u and C, $\phi(u)$ and $\phi(C)$, respectively, before and after the upgrade did
375 not suggest biases were introduced (**Supp. Fig. S7C,7D**). Specifically, changes in the average and median values and
376 in the baseline after 2008 were from better measurement of higher value events (gusts and short positive C anomalies).

377

378 Significant daily to seasonal to interannual variations are apparent in the daily-averaged u and C (**Fig. 3**). The calmest
379 season is late summer to fall, whereas spring is the windiest with greatest variability due to synoptic systems (**Fig.**
380 **3A**). Winds have strengthened since a minimum in 1995-1996, moreso for the seep directions with stronger winds
381 becoming more frequent, moreso summer than winter (**Supp. Figs. S8, S9**).

382

https://doi.org/10.5194/acp-2020-1234
Preprint. Discussion started: 6 July 2021

Atmospheric Chemistry and Physics Discussions

Trends in C reflect trends in both seep field emission and ambient C. C is higher in fall and spring (**Fig. 3B**). Given that stronger winds decrease C through dilution, this suggests the seasonal variation in C underestimates the seasonal variation in emissions. Several studies have shown increased emissions under higher wave regimes (storminess), reviewed in Leifer (2019) and proposed from wave pumping. Storms increase evasion from higher wave turbulence and breaking-wave bubbles, which sparge dissolved CH_4 and other trace gases down to the seabed in shallow (<100 m) waters (Shakhova, Semiletov, Salyuk, et al., 2010). Note, u, θ, and C' correlate with time of day. For example, north generally reflects weak, offshore nocturnal winds with no seep contribution.

3.2.2 Spatial heterogeneity

Calculating the angular-resolved average C, $C_{ave}(\theta)$, for the complete dataset with respect to θ shows the highest C from the main seep field direction (155-250°, **Fig. 4**). For the seep directions, $C_{ave}(\theta)$ was poorly fit by a single Gaussian function but well fit (R^2=0.997) by two Gaussian functions with peaks at 178° and 198° corresponding to the Seep Tent and Trilogy Seeps' directions, respectively (**Fig. 4A, 4B**). Notably, the fit residual showed a linear increasing trend, $dC_{ave}(\theta)/d\theta$, of 0.17 ppb degree^{-1} from 180 to 210° (**Supp. Fig. S9B**) consistent with evasion from a dissolved downcurrent plume that drifts west-northwest along the coast (Leifer, 2019).

The average C anomaly, $C'_{ave}(\theta)$, was calculated from the average of $C_{Obs}(\theta)$ after **Eqn. 1** with terrestrial anthropogenic sources to the north to northeast were removed. The minimum in $C_{Obs}(\theta)$ was at 270°, a direction with no mapped seepage at the dissolved plume's approximate shoreward edge.

There is a strong, focused peak in $C_{max}(\theta)$ at θ~190°, close to the Seep Tent Seep direction (**Fig. 4E, 4F**), which is fairly isolated on the Ellwood Trend (**Fig. 1**). This peak also is close to the direction of Tonya Seep on the Inshore Trend and to the small, unnamed area of seepage to the west of Trilogy Seep along the Red Mtn. Fault trend. The θ-resolved maximum $C(\theta)$, $C_{max}(\theta)$, remains elevated through ~270°, far west of the $C_{ave}(\theta)$ peak at ~200°. This strongly suggests that the seep field extends further to the west-northwest than current maps. These data cannot be explained by dissolved plume outgassing, which would affect $C_{ave}(\theta)$ but not $C_{max}(\theta)$.

$C(\theta)$ enhancements for non-seep directions (**Fig. 4A,4B**) show a peak at ~35°, corresponding to the direction of a commercial center amid suburban development. This could result from terrestrial seepage and natural gas pipeline leakage and/or THC emissions from communities and traffic.

Neglecting the synoptic system, topographic forcing from the east-west Santa Ynez range means that prevailing winds are westerlies, which also are the strongest (**Fig. 4C, 4D**). North winds (320-15°) largely are weak as are winds from due south; however, the sea breeze strengthens winds rapidly away from due south. θ peaks in the maximum winds (1-minute sustained), $u_{max}(\theta)$, correspond to the west and east peaks in $u_{ave}(\theta)$ with strengths to 16 m s^{-1}. Interestingly,

https://doi.org/10.5194/acp-2020-1234
Preprint. Discussion started: 6 July 2021

Atmospheric Chemistry and Physics Discussions

there also are strong north (0-30°) winds or downslope flow, termed sundowner winds, a highly localized and infrequent phenomenon. The overlap of $u_{med}(\theta)$ and $u_{ave}(\theta)$ shows winds largely are normally distributed.

The wind speed probability distribution, $\phi(\theta,u)$, defined:

$$\int^{u} \phi\,(\theta,u)du = 1 \quad (5)$$

varies significantly with direction (**Fig. 5A**). The distribution is very narrow (y-axis) for the northeast (~45°) where winds are largely weak. The distribution is broad for the east-southeast (70-135°) and for the prevailing westerlies (250-280°). The east-southeast distribution skews to the south (stronger winds extend further from the south - offshore), whereas the prevailing westerly wind distribution skews to the northeast (as does the coastline).

The median C, $C_{med}(\theta)$, and average C, $C_{ave}(\theta)$, have similar shapes, albeit with lower values at all θ (**Fig. 4A**), indicating C is not normally distributed. This is shown in the θ-resolved probability distribution of C, $\phi(C,\theta)$ (**Fig. 5B**). In the seep direction, $\phi(C,\theta)$ extends to much higher values than from non-seep directions. $\phi(C,\theta)$ is asymmetric with θ extending further to the west than the seep field extent (240°) and then decreasing more abruptly than the decrease to the east. This asymmetry is expected given the seep field's asymmetric orientation relative to WCS (eastern seepage is more distant). Emissions beyond the field's mapped western edge arise from downcurrent plume outgassing and potentially a contribution from unmapped seeps.

3.2.3 Seep field diurnal emissions cycle

C and u for the seep field direction, u_{seep}, and C_{seep}, respectively, follow diurnal patterns that are not the same as the overall diurnal pattern due to the wind direction constraint and because C_{seep} depends on u_{seep}. The dependency arises because higher u dilutes emissions, decreasing C, but higher u also increases dissolved plume evasion and bubble-mediated emissions from higher swell (after a delay for wave buildup). Diurnal winds in coastal regions feature a shift between weak nocturnal offshore winds that veer to onshore winds in the morning - the sea breeze circulation. This was explored in time and direction segregated u and C and seep direction averaged u_{seep}, and C_{seep} for 90-270° (**Fig. 6**). Data were segregated by θ for pre- and post-2008 (when station improvements facilitated better wind characterization, particularly night time, which are seldom from the seep field direction, see **Supp. Fig. S10** for 1991-2007). $u(\theta,t)$ and $C(\theta,t)$ were 2D Gaussian kernel smoothed with a 1-bin standard deviation (contours based on a 3 bin standard deviation) by the imgaussfilt.m algorithm (MATLAB, MathWorks, MA) after interpolating the calibration data gap 24:00-01:00.

Early morning (01:00–03:00) u_{seep} are stronger because typical nocturnal winds are northerlies (land breeze), coming from the south largely during storms. These are accompanied by elevated C_{seep} implying greater emissions despite enhanced dilution from stronger winds. The minimum in both u_{seep} and C_{seep} occur in the early morning (04:00-08:00),

https://doi.org/10.5194/acp-2020-1234
Preprint. Discussion started: 6 July 2021

Atmospheric Chemistry and Physics Discussions

with both increasing slightly through midday (~12:00). C_{seep} follows an afternoon trend of overall decreasing to a minimum at ~ 20:00 before increasing again into the late evening.

Underlying these trends are complex temporal spatial patterns. u for the north to northeast reaches a maximum around noon and peak around 16:00; while C for northeast to east is low in the morning reaching a peak to the east in the afternoon and likely reflects terrestrial sources. This pattern in $C(t,\theta)$ extends to nearly 130°. Beyond the seep field's western edge, u is elevated from the prevailing direction (270°), with C elevated throughout the morning. There also is a short-lived peak in u around noon at ~300°, which corresponds to a short-lived depressed C. These could be consistent with wave development time, transport time, and sparging of the downcurrent plume; however, interpretation based on these spatial patterns largely is speculative.

3.3 Overall seep field emissions

3.3.1 Overall emissions

Average atmospheric emissions, E_A, for 1990-2020 were derived by an iterative Gaussian plume model, initialized with the 2005 sonar map (**Fig. 1**). An emissions sensitivity study on the effect of grid resolution was conducted for resolutions from 11 to 225 m and a 22/56-m hybrid grid (**Fig. S3**). Simulations used moderate insolation to derive the turbulence parameters and stability class, a 250-m BL (typical Santa Barbara Channel marine values (Edinger, 1959; Rahn, Parish, & Leon, 2017)), and 2° angular resolution (Hanna et al., 1982). Simulations were run iteratively until convergence, typically within 5 iterations (**Supp. Fig. S11**). Simulations used a linear distance weighting function, $K(r,\theta)$, based on sensitivity study (**Supp. Fig. S12**).

Simulations could not reproduce observations in the Platform Holly direction (θ=238°). Thus, a source was added for the platform area, which improved simulation-observational agreement in this wind direction. Since significant seep bubbles plumes generally are not observed in the platform's vicinity, these emissions could arise from incomplete combustion from flaring.

The model-derived, E_A, for 1990-2020 was 83,500 m^3 dy^{-1} (**Fig. 7**). Using a composition-weighted molecular mass of 19.6 g $mole^{-1}$ implies 27 Gg yr^{-1}. Atmospheric seep gas is 88.5% CH_4, implying 19 Gg CH_4 yr^{-1} seep emissions (**Table 1**). Given that CH_4 is 73% of THC, non-methane hydrocarbon (NMHC: C_2-C_7) emissions are 9,500 m^3 dy^{-1}. The largest NMHC was propane with emissions of 3510 m^3 dy^{-1}, followed by ethane at 2590 m^3 dy^{-1}.

Seabed emissions, E_B, are necessarily significantly greater than E_A in the near field as E_A misses the fraction of emissions that remain in the water column, E_W. Note, some of the E_W fraction in the near field evades to the atmosphere in the far field. Clark et al. (2000) estimated a 50:50 air/water partitioning, implying seabed emissions, E_B, 1990-2020 of 167,000 m^3 dy^{-1} or 54 Gg yr^{-1}. A comparison of E_A versus ω showed a very steep increase with ω for E_A = 1-10 g s^{-1} m^{-2} with rollover at ω~0.025 (**Supp. Fig. S13**).

https://doi.org/10.5194/acp-2020-1234
Preprint. Discussion started: 6 July 2021

Atmospheric Chemistry and Physics Discussions

488

489 Insights into the simulations were provided by how the model partitioned emissions between different seep areas.
490 Particularly notable is the model's treatment of the Trilogy Seep area - the second strongest seep area after the Seep
491 Tent Seep - through much of the study period. The model re-assigned Trilogy Seep emissions to seepage to the west,
492 representing Trilogy Seep emissions as unrealistically weaker than other, smaller seeps, such as IV Super Seep. One
493 contributor to this re-assignment is the diurnal cycle. Specifically, morning winds are weaker and from the south and
494 east while afternoon winds are stronger and from the west, thus weaker winds are used to "measure" emissions from
495 the eastern field and stronger winds are used to "measure" emissions from the western field. This could bias emissions
496 (higher for the west and lower for the east) due to an emissions dependency on u – note, wind dilution is addressed by
497 the Gaussian Plume model.
498
499 The model assigned strong emissions to the field's eastern and western edges even though sonar returns here are small.
500 This suggests wind veering plays an important role at the seep area scale. In a comparison of the Seep Tent Seep and
501 La Goleta Seep areas, the model emphasized the Seep Tent Seep whereas La Goleta Seep emissions were shifted to
502 inshore seepage. This re-partitioning was greatly reduced for a +10° wind veer, which also lessened the strengthening
503 of emissions from the field's western edge relative to sonar (**Supp. Fig. S14**). Given the lack of field data between the
504 seep field and WCS on wind veering, further wind veering analysis was not conducted.
505

506 **3.3.2 Seep field sector emissions**

507 To investigate sub-field scale emissions, the seep field was segregated into three sectors: inshore, offshore east, and
508 offshore west (**Fig. 1**). Based on integrating sonar return, ω, the inshore seepage contributes 40% of the field's ω with
509 the offshore seep trend split between 9% for the west and 51% for the east. Supporting this comparison is the similarity
510 in the normalized sonar return probability, $\phi_n(\omega)$, for the inshore seeps and offshore east seeps (**Fig. 8**). In contrast,
511 $\phi_n(\omega)$ for the offshore west seepage differed dramatically despite the similarity in geology along the anticline
512 underlying the offshore seep trend (Leifer et al., 2010). This likely results in part from the interaction between
513 migration and production. Although the normalized atmospheric emissions probability, $\phi_n(E_A)$ for the inshore and
514 offshore seeps are similar over most of the range (except the weakest, E_A<0.02 g s^{-1}), significant differences are evident
515 between offshore east and west seepage. Offshore east seepage is more dispersed and favors weaker seepage compared
516 to offshore west seepage and compared to $\phi_n(\omega)$.
517
518 The weakest seepage (ω<0.02) contributes negligibly to overall emissions and had no notable inshore-offshore
519 difference in $\phi_n(\omega)$. The largest difference is between the strongest seepage (ω>0.5) for the inshore and offshore seeps.
520 Specifically, there is a strong peak at ω~0.45 and nothing stronger for the inshore seeps, whereas offshore $\phi_n(\omega)$
521 continued to larger $\omega \sim 0.7$. The inversion reduced $\phi_n(E_A)$ for the strongest inshore compared to $\phi_n(E_A)$ for strong
522 offshore seepage. Also, $\phi_n(E_A)$ was reduced far more for offshore east seepage than offshore west seepage.
523

https://doi.org/10.5194/acp-2020-1234
Preprint. Discussion started: 6 July 2021


Atmospheric Chemistry and Physics Discussions

These distributions suggest that controlling geological structures (fractures, fault damage zones, and chimneys in the capping Sisquoc Formation) are the same for inshore seepage and offshore east seepage, with the primary difference for the strongest seepage in these two sectors which are of similar strength– the inshore Trilogy Seeps provide focused emissions, whereas the offshore east La Goleta Seeps are comparatively dispersed and far oilier.

Although, ω is not emissions, modeled E_A followed the 40:60 partition in ω between inshore and offshore seepage. Interestingly, the E_A partitioning between the offshore east versus the offshore west differed significantly from partitioning for sonar with 21% from offshore west and 38% from offshore east, i.e., this greatly accentuated the E_A Seep Tent Seep area. In part, this arises from a diurnal cycle bias – WCS observes the offshore west seeps for afternoon/evening westerly winds, which are stronger, whereas WCS observes the offshore east seeps when winds are weaker, earlier in the day (**Fig. 6B**). Winds increase bubble emissions from wave hydrostatic pumping and dissolved gas evasion. Also potentially contributing is saturation of ω at very high bubble-density bubble plumes, such as the Seep Tent Seep and Trilogy Seep (Leifer et al., 2017). Saturation would imply an under-estimate of ω for the strongest seep area emissions.

3.3.3 Uncertainty and emissions sensitivity

Given the number of sources of variability that are poorly characterized by available data, uncertainty would be best assessed by Monte Carlo simulations; however, this was unfeasible due to the simulations' computational demands. Thus, emissions uncertainty was investigated by sensitivity studies (**Fig. 9**). Where data were available, uncertainty due to a specific parameter was estimated from these simulations. Specific factors studied included sonar resolution, angular resolution, $\delta\theta$, wind speed, u, concentration anomaly, C', boundary layer height, BL, wind veering, ψ, spatial northing offset, Y, and the inshore and offshore seepage partitioning, ζ. Sensitivity studies are detailed in **Supp. Sec. S7.4.**

The contribution to uncertainty from $\delta\theta$, C', ψ, and spatial offsets within the seep trends were minimal – just a few percent or less, as was uncertainty associated with u due to BL sensitivity countering u sensitivity. Moderate uncertainty was identified for BL and ζ. For BL ranging from 150 to 350 m, mean E_A uncertainty was 6%. Assessing uncertainty in ζ was more challenging as there is no verification data on variability in the E_A partitioning between the inshore and offshore seep trends. Still, the mean E_A uncertainty for $-50\% < \zeta < 50\%$ is 11.5% from a polynomial fit. Whereas ζ could be larger, there is consistency in seepage location between sonar surveys spanning decades (Leifer, 2019), which suggests that averaged changes in ζ on multi-decade timescales are modest. Total uncertainty was taken as 15% based on the sum of uncertainty in BL and ζ.

https://doi.org/10.5194/acp-2020-1234
Preprint. Discussion started: 6 July 2021

Atmospheric Chemistry and Physics Discussions

3.4 Ellwood Field emissions

$C(\theta)$ increases to the northeast with a peak at 290-320° corresponding to the direction towards abandoned wells off Haskell Beach (**Fig. 10**). Emissions from this area – either from seepage or leaking wells also were noted in the offshore survey data near Haskell Beach (**Fig. 2A**). Additionally, $C_{max}(\theta)$ shows a 22-ppm peak in in this direction (**Fig. 4F**), also consistent with natural seepage or well leakage.

Ellwood field production continued through the 1970s with wells drilled into the geological structures that allowed oil accumulation (Olson, 1983) but also provided migration pathways (Leifer et al., 2010). There are many abandoned wells from these fields and others fields in the Goleta Plains, beaches, and shallow near-coastal water to the west-northwest of WCS (offshore Haskell Beach and onshore around Naples Point). Currently, active wells only are found at the La Goleta Gas field (a natural gas storage field), east of WCS.

Faults associated with these anticlines provide migration pathways and are aligned approximately with the coast in a series of roughly parallel faults extending onshore (Minor et al., 2009). The onshore/coastal Ellwood field (northwest of the South Ellwood field) sources from the primarily sandstone Vaqueros Formation (Olson, 1983), whose main trap is an anticline at the western edge of the North Branch Western More Ranch Fault (NBWMRF). Offshore seepage tracks some of these faults, e.g., the Isla Vista Fault trend corresponds to an offshore seep trend in Goleta Bay that includes the Goleta Pier Seep, whereas wells follow the NBWMRF trend offshore of Haskell Beach.

4 Discussion

4.1 Atmospheric seep field observations

4.1.1. Air quality station

A range of approaches are available to evaluate marine seepage CH_4 emissions: *in situ* approaches including direct capture (Leifer, 2015; Washburn, Johnson, Gotschalk, & Egland, 2001), fluid flow measurements (Leifer & Boles, 2005), video (Leifer, 2015), and remote sensing approaches that include active acoustics, i.e., sonar (Hornafius et al., 1999), dissolved *in situ* (Marinaro et al., 2006), and passive acoustics (Wiggins et al., 2015). Remote sensing is the best approach for long-term monitoring to capture emissions shifts between vents. To date, only sonar remote sensing has provided quantitative seep plume (seabed) emissions. Notably, sonar ranges are up to a few hundred meters, far less than the size scales of many seep fields, while high power-demands typically require a cabled observatory for long-term observations.

This study demonstrated that air quality station data provides the long-term continuous data needed to capture seasonal variations including emissions during storms and transient events, which field campaigns likely miss. For example,

https://doi.org/10.5194/acp-2020-1234
Preprint. Discussion started: 6 July 2021

sonar surveys tend to occur during summer when seas are calmer and more predictable but when seepage is weakest (**Fig. 3**), remaining in port during storms when emissions are enhanced.

The approach derived atmospheric trace gas emissions for a dispersed area source constrained by sonar seepage maps from long-term air quality and meteorology data. This approach can be extended to terrestrial seepage if the source can be constrained spatially (due to geology); although nearby anthropogenic sources may complicate emissions assessment. Other terrestrial sources such as landfills, O&G production fields, or industrial sites – if spatially constrained – could be addressed by this approach. The use of cavity enhanced absorption spectrometers that can speciate gases like CH_4 and C_2H_6 could enable discrimination of confounding sources as well as better characterization of emissions. Although an onshore station can address nearshore seepage, further offshore seepage could be addressed by a moored station. A moored station could also support *in situ* aqueous chemical sensors, current measurements.

4.1.2 *In situ* atmospheric surface surveys

Atmospheric emissions were assessed for three seep areas by an atmospheric *in situ* survey approach wherein downwind data are collected orthogonal to the wind direction in a transect that spans the plume (background to background on the plume's edges). This approach was developed for terrestrial sources (Leifer, Melton, Tratt, et al., 2018) yet largely has not been used for offshore marine seepage, which often are area sources. In this study, this was addressed by gridding the area source and treating each grid as a far field point source. Gaussian plume inversion requires distant source(s), i.e., far field. Surveys of three strong seep areas all were well characterized by the Gaussian plume model.

One advantage of atmospheric surveys is rapidity - a single transect of a few minutes is sufficient to derive emissions for a seep area. In comparison, a flux buoy survey can require many hours to a day (Clark et al., 2010), during which forcing factors (waves, tides, etc.) change significantly. Also rapid are seep area sonar surveys (Wilson, Leifer, & Maillard, 2015) allowing a combined sonar and atmospheric survey to repeat characterize emissions and sea-air partitioning within a few hours. With respect to the entire COP seep field, whereas a sonar survey requires two to three days (Leifer et al., 2010), a downwind atmospheric survey is far more rapid, requiring perhaps an hour. This allows repeat field emissions measurements over a tidal cycle.

4.2 Seep field emissions

4.2.1 Total emissions

To date, only two estimates of COP seep field seabed emissions, E_B, have been published. Hornafius et al. (1999) estimated E_B=1.5x10^5 m^3 dy^{-1} (64 Gg yr^{-1}) based on sonar surveys covering 18 km^2 from Nov. 1994 – Sep. 1996, collected during the summer to late fall seasons. This value excluded Seep Tent collection. A 4.1 km^2 sonar survey in Aug.-Sep. 2016 estimated E_B=24,000 m^3 dy^{-1} (Padilla, Loranger, Kinnaman, Valentine, & Weber, 2019), significantly

https://doi.org/10.5194/acp-2020-1234
Preprint. Discussion started: 6 July 2021


Atmospheric Chemistry and Physics Discussions

lower, which in part arises from field subsampling, but also could arise from long-term changes; however, neither study addressed temporal variability. The sonar surveys occurred in summer and fall when seepage activity is at a minimum, whereas winter and early spring feature much higher activity associated with large transient events and storms (Bradley et al., 2010).

Hornafius et al. (1999) used an engineered bubble plume to calibrate emissions, an approach also used in Leifer et al. (2017). Due to technology limitations at the time, the strongest seepage was clipped or saturated, i.e., underestimated, and the survey did not cover shallow seepage. Thus, the Hornafius et al. (1999) emissions estimate is a lower limit for summer/fall emissions. The Padilla et al. (2019) survey was calibrated by an inverted seep flux buoy suspended at 23 m. This differs significantly from seep flux buoy measurements (Washburn et al., 2001), which are collected in surface drift mode. Surface drift mode ensures a horizontal orientation for the buoy and an absence of lateral velocity difference between the capture device and currents – either of which decreases capture efficiency from 100%, biasing derived emissions low. Further, the Padilla et al. (2019) survey was calibrated 1 month after the sonar surveys, whereas the 1995 engineered plume calibration by Hornafius et al. (1999) was contemporaneous. The Hornafius et al. (1999) approach accounts (partially) for dissolution between the seabed and survey depth window, albeit air dissolves slower than methane. Dissolution losses between the seabed and the depth window can be addressed by a numerical bubble model (Leifer et al., 2017).

Based on the Gaussian plume model-derived E_A was 8.4×10^4 m^3 dy^{-1}, which based on a Clark et al. (2000) assessment that half the seabed seepage reaches the atmosphere, suggests E_B=1.7×10^5 m^3 dy^{-1}; very similar to E_B=1.5×10^5 m^3 dy^{-1} from Hornafius et al. (1999). This agreement is coincidental as it neglects seasonal and interannual trends. For example, Bradley et al. (2010) found 1994-1996 emissions were well below the average for 1990-2008, increasing significantly after 2008.

4.2.2 Methane and non-methane hydrocarbon emissions

Analysis of atmospheric samples provided a picture of the complexity of atmospheric emissions that arises from the multiple pathways underlying atmospheric emissions. Specifically, as bubbles rise, they lose lighter and more soluble gases faster (deeper in the water column), leading to differences between evasion from dissolved gases and direct bubble transport (Leifer & Clark, 2002). Thus, bubble-mediated transport enhances larger alkanes relative to smaller alkanes leaving more of the smaller alkanes in the water column. For strong seeps, bubble plumes are associated with strong upwelling flows (Leifer et al., 2009), which transport dissolved gases to the sea surface where they can outgas. Additionally, oil (as droplets and bubble coatings) enhances alkane transport due to slower dissolution and diffusion of larger alkanes through oil.

Atmospheric plume concentrations were 11.5% NMHC and 88.5% CH_4, very similar to Hornafius et al. (1999) who referenced the Seep Tent composition (88% CH_4, 10% NMHC, and 2% nitrogen) as very similar to the reservoir

https://doi.org/10.5194/acp-2020-1234
Preprint. Discussion started: 6 July 2021

Atmospheric Chemistry and Physics Discussions

composition. Note, Clark et al. (2010) observed Trilogy near sea surface bubbles with 5.7% to 7.9% NMHC and 52.4 to 79.7% CH_4, demonstrating significant partitioning. The similarity between the atmospheric and seabed composition demonstrates efficient dissolved gas transfer to the sea surface.

COP seep field seabed emissions are orders of magnitude greater than typically reported for other seep areas, e.g., summary Römer et al. (2017) where emissions for 12 different seep areas including for sites in the North Sea, Pacific north west, Gulf of Mexico, etc., were 2-480 tons yr^{-1}, multiple orders of magnitude less than seabed emissions for Coal Oil Point. Römer et al. (2017) for Dogger Bank in the North Sea observed atmospheric CH_4 plumes and estimated direct atmospheric bubble-mediated transfer using a bubble model to suggest 20% of seabed emissions directly reached the atmosphere 21.7 ton yr^{-1}. For the Tommelieten Seeps in 70-m water Schneider von Deimling et al. (2011) estimated 4% of the 0.024 Gg CH_4 yr^{-1} seabed emissions, i.e., ~1 Mg CH_4 yr^{-1} reached the atmosphere by bubble-mediated transfer. Schneider von Deimling et al. (2011) used a bubble model based on an assumed bubble size and neglected diffusive flux. These diffusive fluxes include bubble dissolution into the wave mixed layer in the local area. A few studies have directly measured atmospheric fluxes by an air-sea gas transfer model. For example, Schmale, Beaubien, Rehder, Greinert, and Lonmbardi (2010) found seep air fluxes of 0.96-2.32 nmol m^{-2} s^{-1}, much higher than the ambient Black Sea flux of 0.32-0.77 nmol m^{-2} s^{-1}. In the Black Sea, ambient emissions arise from microbially produced CH_4 in shelf and slope sediments (Reeburgh et al., 1991). Di, Feng, and Chen (2019) estimated 7.7 nmol m^{-2} s^{-1} for the shallow South China Sea based on an air-sea gas transfer model. If we disperse COP seep field atmospheric emissions of $1.15x10^9$ M yr^{-1} over the ~6.3 km^2 of 25x25 m^2 bins with emissions, we find 5.7 µM m^{-2} s^{-1}, three orders of magnitude greater.

Recent estimates of total global geo-CH_4 sources from a bottom-up approach are 45 Tg yr^{-1} with submarine seepage contributing 7 Tg yr^{-1} (Etiope & Schwietzke, 2019), implying COP seep field contributes 0.25% of the bottom-up submarine emissions. However, an estimate of pre-industrial CH_4 emissions (not confounded with fossil fuel production emissions) based on ice core $^{14}CH_4$ suggested 1.6 Tg geo-CH_4 yr^{-1} emissions (Hmiel et al., 2020). This estimate, if accurate, suggest the COP seep field contributes an astounding 1% of global seep emissions (submarine and aerial) and is difficult to reconcile with the COP seep field and other top seepage estimates. For example, CH_4 atmospheric emissions for the Lusi hydrothermal system of 0.1 Tg yr^{-1} (Mazzini et al., 2021), a hotspot in the Laptev Sea of 0.9 Tg yr^{-1} into shallow seas (Shakhova, Semiletov, Leifer, et al., 2010), and for the East Siberian Arctic Sea using eddy covariance of 3.0 Tg yr^{-1}(Thornton et al., 2020). Thus, COP seep field emissions either play a significant role in global seep emissions or indicate that geo-gas emissions are less tightly constrained.

COP seep field C_2H_6 emissions were 1.27 Gg C_2H_6 yr^{-1}. For reference, this is 11% of the 11.4 Gg C_2H_6 yr^{-1} in 2010 for the South Coast Air Basin (SCAB), which includes Los Angeles (Peischl et al., 2013). Globally, Simpson et al. (2012) and Höglund-Isaksson (2017) found 11.3 and 9.7 Tg C_2H_6 yr^{-1} in 2010, respectively. C_2H_6 has been increasing since 2010 due to increased O&G production emissions (Helmig et al., 2016). Globally, seeps are estimated to

https://doi.org/10.5194/acp-2020-1234
Preprint. Discussion started: 6 July 2021

Atmospheric Chemistry and Physics Discussions

contribute 2-4 Tg C_2H_6 yr^{-1} (Etiope & Ciccioli, 2009), and from ice cores, 2.2-3.5 Tg yr^{-1}(Nicewonger, Verhulst, Aydin, & Saltzman, 2016), suggesting the seep field contributes 0.03-0.06% of global seep emissions.

Seep THC was 4.2% propane, implying emissions of 2.5 Gg C_3H_8 yr^{-1}. Global propane emissions are 10.5 Tg yr^{-1} (Pozzer et al., 2010), with 1-2 Tg yr^{-1} estimated for seeps (Etiope & Ciccioli, 2009). Thus, the COP seep field could contribute 0.05-0.1% of the global seep budget. Oceans are estimated to contribute 0.35 Tg C_3H_8 yr^{-1} (Pozzer et al., 2010), less than geological seepage.

Global butane emissions are 14 Tg C_4H_{10} yr^{-1} (Pozzer et al., 2010), higher than ethane and propane. COP seep field butane (C_4) and pentane (C_5) emissions were 2.2 Gg C_4H_{10} yr^{-1} and 1.1 Gg C_5H_{12} yr^{-1}, respectively, thus combined C_2-C_5 emissions are 7.1 Gg yr^{-1}, compared to 65 Gg yr^{-1} from the entire SCAB, i.e., COP seep field contributes ~5% the SCAB. COP C_2-C_5 emissions are significantly above that of the La Brea area, estimated at 1.7 Gg yr^{-1} (D. Weber et al., 2017). Note, COP seep field atmospheric C_2-C_5 emissions certainly are larger, potentially significantly, as higher alkanes also are emitted from oil slicks, whose downcurrent contributions were not considered for this study and atmospheric plume was not sampled for this study.

Both benzene and toluene were detected with estimated emissions of 5000 and 1300 kg yr^{-1}, respectively. These emissions likely are underestimates, potentially significantly, due to neglecting the contribution from oil slicks. Both gases are of significant health concerns.

Based on evaluating the COP seep field with respect to global seep ethane and propane emissions, COP seep field contribution to global geo-CH_4 emissions (in parentheses) are consistent with recent global geo-gas CH_4 emissions estimates of 45 Tg yr^{-1} (0.04%) (Etiope et al., 2019), but not the significantly lower pre-industrial estimates of global geo-CH_4 emissions, e.g., 1.6 Tg yr^{-1} (1.15%) (Hmiel et al., 2020).

4.3 Downcurrent emissions

The seep field concentration, $C'(\theta)$, anomaly was centered at θ~200° and was well described by a dual Gaussian function (**Fig. 4B**). This was surprising given that the seep field is asymmetric with respect to a 200° axial line from WCS to COP. Underlying this seeming discrepancy is that WCS winds are weakest from due south and strongest from the west (prevailing) and also stronger to the east-southeast (**Fig. 4C**).

The residual of the Gaussian fit increased in the downcurrent direction (**Supp. Fig. S9B**), consistent with evasion from the downcurrent dissolved plume plus and seepage from this area. The dissolved plume roughly follows the coast, extending as far as ~280° from WCS due to the coastline shift from northwest to west around Haskell Beach (**Fig. 2**), ~30° beyond the seep field's sonar mapped western edge (**Fig. 1**). As prevailing winds are westerlies (paralleling the coastal mountains), downcurrent plume evasions decrease with distance as surface waters become depleted by evasion.

https://doi.org/10.5194/acp-2020-1234
Preprint. Discussion started: 6 July 2021


Atmospheric Chemistry and Physics Discussions

733 Evasion increases non-linearly with *u*, particularly for winds that include wave breaking (Nightingale et al., 2000);
734 however, higher winds also dilute emissions more. Note, there are no mapped seeps in this area.
735
736 A similar situation likely occurs towards the east and leads the model to emphasize seepage at the field's eastern
737 extent, too. Specifically, strong prevailing afternoon westerly surface winds drive a near-surface dissolved plume
738 eastwards. When these westerly winds calm down late in the evening, easterly winds will transport evasion from this
739 east-displaced dissolved plume towards WCS. Additionally, it also is possible that the COP seep field extends further
740 east than mapped in sonar surveys, at least during some seasons.
741

742 **4.4 Focused seep area emissions**

743 Trilogy Seep area emissions were estimated at 6,200 m^3 CH_4 dy^{-1} in May 2016. For comparison, Clark et al. (2010)
744 found 5500 and 4200 m^3 THC dy^{-1} (4,900 and 3,700 m^3 CH_4 dy^{-1}) for Trilogy Seep as measured by flux buoy for near
745 surface bubble fluxes in Sept. 2005. Note, the plume inversion approach also includes outgassing of near surface
746 waters that have enhanced C_{CH4} from plume dissolution, the flux buoy approach does not. Although Clark et al. (2010)
747 found surface bubbles had undetectable CO_2, the atmospheric plume's CO_2 to CH_4 concentration ratio was comparable
748 to the seabed bubble concentration ratio. This demonstrates significant upwelling flow transport of seabed water to
749 the sea surface where dissolved gases evade near where the bubble plume surfaces. This near-plume evasion
750 contributes to the atmospheric plume surveyed by the *in situ* measurements. Note, these emissions neglect
751 downcurrent emissions. A 50:50 atmosphere/ocean partitioning suggests 2016 Trilogy Seep emissions were ~40%
752 lower than in 2005 – a difference within the difference between the two 2005 Trilogy Seep measurements Clark et al.
753 (2010).
754
755 In contrast, there was very poor agreement for the Seep Tent Seep, for which Clark et al. (2010) mapped emissions of
756 5700 m^3 day^{-1} (5000 m^3 CH_4 day^{-1}) in Nov. 2002 whereas this study found 310 m^3 CH_4 dy^{-1}. This discrepancy was
757 readily apparent with almost no visible surface bubble expression in May 2016, whereas the Seep Tent Seep has been
758 a perennial feature since its appearance. The absence of more than a few scattered bubbles at the sea surface (the boil
759 in 2000 was driven by a 1-2 m s^{-1} upwelling - Leifer, Clark, and Chen (2000)) indicates that most emissions are from
760 evasion. A buoyancy plume associated with the rising oil (thick oil slicks surface above the Seep Tents) as well as
761 methane dissolved in the oil likely is transporting the observed, focused CH_4 emissions.
762
763 This is remarkable given that the seep field's geofluid migration "center" in recent decades has been the Seep Tent
764 Seep (Bradley et al., 2010), which was the largest seep in the field in 2010 (Clark et al., 2010). The Seep Tent Seep
765 consists of emissions not captured by the Seep Tents – two large (33 m square) steel capture tents on the seafloor. For
766 reference, the Seep Tents captured ~16,800 m^3 gas dy^{-1} in the early 2000s (Boles et al., 2001). Bradley et al. (2010)
767 found in WCS data that when overall seep field emissions decreased to a minimum in 1995, they were focused on the

https://doi.org/10.5194/acp-2020-1234
Preprint. Discussion started: 6 July 2021


Atmospheric Chemistry and Physics Discussions

768 Seep Tent Seep direction. Note, the Seep Tent Seep was observed first in 1970 as a boil visible from 1.6-km distant.
769 The seepage was tented in Sept. 1982 (Boles et al., 2001).
770
771 Underlying these observations are several factors. First, the Seep Tent Seep is modern – since 1978 – as it was not
772 mapped in a 1953 seep survey (Leifer, 2019). At the time it was first reported as a sea boil visible over a kilometer
773 distant (Boles et al., 2001). Since installation, overall Seep Tent production has diminished (Boles et al., 2001) by a
774 factor of 3 from 1984 to 1995. Some fraction of this trend could have resulted from the expansion of active seepage
775 beyond the seep tents. Perhaps more significantly, the Seep Tent Seep lies over one of the Platform Holly wells (Leifer
776 et al., 2010; Fig. 3C), creating the potential of linkage between well production (including stimulation) and Seep Tent
777 production and thus Seep Tent seepage (the uncaptured portion). The near cessation of Seep Tent Seep emissions in
778 the field observations is consistent with a positive relationship between the two.
779

780 **4.6 Diurnal trend and bias**

781 The diurnal wind patterns typical of the coastal Pacific marine environment are weak offshore (northerly) night winds
782 that shift to from the east in the morning and then from the south. In afternoon they strengthen and shift to prevailing
783 westerlies, extending late into the night (Bradley et al., 2010). Note, WCS seep emissions require winds to "probe or
784 scan" across the seep field, and thus miss the strong afternoon prevailing winds when emissions are higher.
785 Specifically, higher wind speeds increase sea-air gas emissions of dissolved near-surface gases (Nightingale et al.,
786 2000) and increase emissions from higher hydrostatic pressure fluctuation driven by wave height (Leifer & Boles,
787 2005). Given that prevailing winds are westerlies, higher afternoon emissions will generally (but not always) drift
788 eastwards, missing WCS.
789
790 The diurnal wind pattern from the seep field direction is different from the overall (direction-independent) diurnal
791 pattern. Typical nocturnal winds are quite weak, 1.5–1.7 m s^{-1} (**Fig. 6**). The strongest diurnal wind change was from
792 late night to morning: a 20% decrease. Onshore winds (seep direction) in the middle of the night are from synoptic
793 systems and were associated with the highest *C'*. Winds increase by a few percent to an early afternoon peak,
794 decreasing through early evening before rising into the night.
795
796 The *C* seep direction trend followed the diurnal wind cycle, increasing by ~20 ppb peaking ~2 hours later in the day
797 than winds (15:00 versus 13:00 for *C* compared to *u*, respectively), which likely reflects wave height (which lags wind
798 strengthening due to the time for wave development) and transport time. Based on sensitivity studies, the diurnal
799 cycles in *u* and *C* correspond to variations of ~7% and ~9% in E_A.
800
801 Although efforts were made to characterize the diurnal cycle from WCS data, WCS data poorly samples the seep field
802 for the higher wind speeds that occur in the afternoon which primarily are westerlies. Note, non-linearity in sea-air
803 evasion with *u* means the model use of average *u* underestimates E_A. Thus, the contribution of the prevailing afternoon

https://doi.org/10.5194/acp-2020-1234
Preprint. Discussion started: 6 July 2021

winds to diurnal emissions is significantly underestimated from WCS data. It is worth noting, though, that this factor only affects 25-33% of diurnal emissions. As the true diurnal cycle cannot be derived from WCS data, field data of repeat transects spanning the different phases of a diurnal cycle are needed.

4.7 Future needs and improvements

The sensitivity studies identified areas for improvement and data gaps. These are described in brief below and in more detail in **Supp. Sec. S8**. The largest uncertainty was with regards to partitioning between the inshore and offshore seep trends, which could be determined by a second air quality station, preferably including speciation such as by CEAS analyzers of CH_4 and C_2H_6. Another important sensitivity was to boundary layer height, *BL*, which varies diurnally and seasonally (Dorman & Winant, 2000) and could be derived from ceilometer data (Münkel, 2007). Another concern is afternoon emissions when seep field emissions bypass WCS, which could be addressed by field work and a second air quality station at a different downwind direction from the seep field.

The model was limited by available workstation power; however, additional computation power could open improvements such as simulating a range of wind speeds. Mapping offshore wind veering in the seep field would open simulations to provide insights at the seep area scale. Further simulations could add grid cells for evasion corresponding to the downcurrent plumes to assess their contribution.

5 Conclusions

In this study, data from an onshore air quality station located downwind of a large marine seep field was analyzed to derive the three-decade-averaged seep field emissions using an inversion model. The modeled emissions were similar to reported emissions; however, this was coincidental given that prior reported emissions were during a period of field quiescence. Highlighting the significance of the COP seep field, ethane and propane emissions suggest the COP seep field contributes 0.04% and 0.12% of the global seep budget, respectively. As a result, COP seep field emissions of 19 Tg CH_4 yr^{-1} are consistent with global geo-gas budgets of 45 Tg yr^{-1}, but inconsistent with significantly lower emissions estimated from ice core isotopic data. Additionally, the approach could be adapted to air quality station data for other sources including terrestrial seeps, production fields, etc., if the sources are spatially constrained.

Data availability. All data needed to evaluate the conclusions in the paper are present in the paper and/or the Supplementary Materials and/or were submitted to the Mendeley Data Repository, see Leifer, Ira (2020), "Seep_Air_Data", Mendeley Data, V1, http://dx.doi.org/10.17632/znzhxkftm8.1

Supplement. The supplement contains additional supporting figures and details to complement the manuscript and an interactive map file as a Google Earth archive of the offshore survey data that are presented in **Fig. 2**.

https://doi.org/10.5194/acp-2020-1234
Preprint. Discussion started: 6 July 2021

Atmospheric Chemistry and Physics Discussions

839 **Author Contributions.** IL Developed and conducted the study, analysed data, and wrote the manuscript. CM analysed
840 data and edited the manuscript. DB analysed air sample data and edited the manuscript.
841
842 **Competing interests.** The authors declare that they have no conflict of interest.
843
844 **Acknowledgements.** We would like to gratefully acknowledge the SBCAPCD for providing data from their ongoing
845 monitoring program and the contribution of Marc Moritsch and Joel S. Cordes in particular for help with these data,
846 and Doug Wilson for the processed sonar data. We recognize the skill and participation of vessel captains Jeff Wright
847 and Tony Vultaggio and editorial review by Charlotte Marston, Bubbleology Research International.
848
849 **Financial Support.** This work was supported by Plains All American Pipeline and the Bubbleology Research
850 International, Internal Research and Development (IRAD) fund.
851

https://doi.org/10.5194/acp-2020-1234
Preprint. Discussion started: 6 July 2021

Atmospheric Chemistry and Physics Discussions

852 **References**

853 Abrams, M. A. (2005). Significance of hydrocarbon seepage relative to petroleum generation and
854 entrapment. *Marine and Petroleum Geology, 22*(4), 457-477.
855 doi:10.1016/j.marpetgeo.2004.08.003
856 Abrams, M. A. (2017). Evaluation of near-surface gases in marine sediments to assess
857 subsurface petroleum gas generation and entrapment. *Geosciences, 7*(2), 35.
858 doi:10.3390/geosciences7020035
859 Bernard, B. B., Brooks, J. M., & Zumberge, J. (2001, 16-19 September 2001). *Determining the*
860 *origin of gases in near-surface sediments.* Paper presented at the AAPG Hedberg
861 Conference, Vancouver BC, Canada.
862 Boles, J. R., Clark, J. F., Leifer, I., & Washburn, L. (2001). Temporal variation in natural
863 methane seep rate due to tides, Coal Oil Point area, California. *Journal Geophysical*
864 *Research - Oceans, 106*(C11), 27,077-027,086. doi:10.1029/2000JC000774
865 Borges, A. V., Champenois, W., Gypens, N., Delille, B., & Harlay, J. (2016). Massive marine
866 methane emissions from near-shore shallow coastal areas. *Scientific Reports, 6*, 27908.
867 doi:10.1038/srep27908
868 Bradley, E. S., Leifer, I., & Roberts, D. A. (2010). Long-term monitoring of a marine geologic
869 hydrocarbon source by a coastal air pollution station in Southern California. *Atmospheric*
870 *Environment, 44*(38), 4973-4981. doi:10.1016/j.atmosenv.2010.08.010
871 CDOGGR. (2018). Well Finder. Retrieved from
872 https://www.conservation.ca.gov/dog/Pages/Wellfinder.aspx. Retrieved 6 May 2019,
873 from California Department of Conservation
874 https://www.conservation.ca.gov/dog/Pages/Wellfinder.aspx
875 Clark, J. F., Washburn, L., Hornafius, J. S., & Luyendyk, B. P. (2000). Natural marine
876 hydrocarbon seep source of dissolved methane to California coastal waters. *Journal*
877 *Geophysical Research - Oceans, 105*, 11,509-511,522. doi:10.1029/2000JC000259
878 Clark, J. F., Washburn, L., & Schwager, K. (2010). Variability of gas composition and flux
879 intensity in natural marine hydrocarbon seeps. *Geo-Marine Letters, 30*, 379-388.
880 doi:10.1007/s00367-009-0167-1
881 Di, P., Feng, D., & Chen, D. (2019). The distribution of dissolved methane and its air-sea flux in
882 the plume of a seep field, Lingtou Promontory, South China Sea. *Geofluids, 2019*,
883 3240697. doi:10.1155/2019/3240697
884 Di, P., Feng, D., Tao, J., & Chen, D. (2020). Using time-series videos to quantify methane
885 bubbles flux from natural cold seeps in the South China Sea. *Minerals, 10*(3), 216.
886 doi:10.3390/min10030216
887 Dorman, C. E., & Winant, C. D. (2000). The structure and variability of the marine atmosphere
888 around the Santa Barbara Channel. *Monthly Weather Review, 128*(2), 261-282.
889 doi:10.1175/1520-0493(2000)128<0261
890 Edinger, J. G. (1959). Changes in the depth of the marine layer over the Los Angeles Basin.
891 *Journal of Meteorology, 16*(3), 219-226. doi:10.1175/1520-
892 0469(1959)016<0219:citdot>2.0.co;2
893 Etiope, G., & Ciccioli, P. (2009). Earth's degassing: A missing ethane and propane source.
894 *Science, 323*(5913), 478-478. doi:10.1126/science.1165904
895 Etiope, G., Ciotoli, G., Schwietzke, S., & Schoell, M. (2019). Gridded maps of geological
896 methane emissions and their isotopic signature. *Earth System Science Data, 11*(1), 1-22.
897 doi:10.5194/essd-11-1-2019

https://doi.org/10.5194/acp-2020-1234
Preprint. Discussion started: 6 July 2021

898 Etiope, G., & Schwietzke, S. (2019). Global geological methane emissions: An update of top-
899 down and bottom-up estimates. *Elementa: Science of the Anthropocene, 7*.
900 doi:10.1525/elementa.383
901 Fischer, P. J. (1978). Oil and Tar Seeps, Santa Barbara Basin, California. In D. J. Everitts, R. G.
902 Paul, C. F. Eaton, & E. E. Welday (Eds.), *California Offshore Gas, Oil and Tar Seeps*
903 (pp. 1-62). Sacramento, California: California State Lands Commission.
904 Freeworldmaps (Cartographer). (2020). Physical Map of California. Retrieved from
905 https://www.freeworldmaps.net/united-states/california/map.html
906 Frew, N. M., Bock, E. J., Schimpf, U., Hara, T., Haußecker, H., Edson, J. B., . . . Jähne, B.
907 (2004). Air-sea gas transfer: Its dependence on wind stress, small-scale roughness, and
908 surface films. *Journal of Geophysical Research: Oceans, 109*(C8), C08S17.
909 doi:10.1029/2003JC002131
910 Greinert, J. (2008). Monitoring temporal variability of bubble release at seeps: The
911 hydroacoustic swath system GasQuant. *Journal of Geophysical Research, 113*, C07048.
912 doi:10.1029/2007JC004704
913 Greinert, J., McGinnis, D. F., Naudts, L., Linke, P., & De Batist, M. (2010). Atmospheric
914 methane flux from bubbling seeps: Spatially extrapolated quantification from a Black Sea
915 shelf area. *Journal of Geophysical Research, 115*. doi:10.1029/2009jc005381
916 Hanna, S. R., Briggs, G. A., & Hosker Jr., R. P. (1982). *Handbook on Atmospheric Diffusion* (J.
917 S. Smith Ed.): Technical Information Center, U.S. Department of Energy.
918 Helmig, D., Rossabi, S., Hueber, J., Tans, P., Montzka, S. A., Masarie, K., . . . Pozzer, A. (2016).
919 Reversal of global atmospheric ethane and propane trends largely due to US oil and
920 natural gas production. *Nature Geoscience, 9*(7), 490-495. doi:10.1038/ngeo2721
921 Heyer, J., & Berger, U. (2000). Methane emission from the coastal area in the Southern Baltic
922 Sea. *Estuarine, Coastal and Shelf Science, 51*(1), 13-30. doi:10.1006/ecss.2000.0616
923 Higgs, B., Mountjoy, J. J., Crutchley, G. J., Townend, J., Ladroit, Y., Greinert, J., & McGovern,
924 C. (2019). Seep-bubble characteristics and gas flow rates from a shallow-water, high-
925 density seep field on the shelf-to-slope transition of the Hikurangi subduction margin.
926 *Marine Geology, 417*, 105985. doi:10.1016/j.margeo.2019.105985
927 Hmiel, B., Petrenko, V. V., Dyonisius, M. N., Buizert, C., Smith, A. M., Place, P. F., . . .
928 Dlugokencky, E. (2020). Preindustrial 14CH4 indicates greater anthropogenic fossil CH4
929 emissions. *Nature, 578*(7795), 409-412. doi:10.1038/s41586-020-1991-8
930 Höglund-Isaksson, L. (2017). Bottom-up simulations of methane and ethane emissions from
931 global oil and gas systems 1980 to 2012. *Environmental Research Letters, 12*(2), 024007.
932 doi:10.1088/1748-9326/aa583e
933 Hornafius, S. J., Quigley, D. C., & Luyendyk, B. P. (1999). The world's most spectacular marine
934 hydrocarbons seeps (Coal Oil Point, Santa Barbara Channel, California): Quantification
935 of emissions. *Journal Geophysical Research - Oceans, 104*(C9), 20,703-720,711.
936 doi:10.1029/1999JC900148
937 Hughes, M., Hall, A., & Fovell, R. G. (2007). Dynamical controls on the diurnal cycle of
938 temperature in complex topography. *Climate Dynamics, 29*(2), 277-292.
939 doi:10.1007/s00382-007-0239-8
940 IEA. (2020). *Methane Tracker 2020*. Retrieved from Paris: https://www.iea.org/reports/methane-
941 tracker-2020

https://doi.org/10.5194/acp-2020-1234
Preprint. Discussion started: 6 July 2021

Atmospheric Chemistry and Physics Discussions

IPCC. (2013). *Working Group 1 Contribution to the IPCC Fifth Assessment Report Climate Change 2013-The Physical Science Basis*. Retrieved from IPCC Secretariat, Geneva, Switzerland:

IPCC. (2014). *Climate Change 2014: Synthesis Report. Contributions of Working Groups I, II and III to the Fifth Assessment Report of the Intergovernmental Panel on Climate Change*. Retrieved from Geneva, Switzerland: http://www.ipcc.ch/pdf/assessment-report/ar5/syr/SYR_AR5_FINAL_full_wcover.pdf

Jackson, R. B., Saunois, M., Bousquet, P., Canadell, J. G., Poulter, B., Stavert, A. R., . . . Tsuruta, A. (2020). Increasing anthropogenic methane emissions arise equally from agricultural and fossil fuel sources. *Environmental Research Letters, 15*(7), 071002. doi:10.1088/1748-9326/ab9ed2

Johansen, C., Macelloni, L., Natter, M., Silva, M., Woosley, M., Woolsey, A., . . . MacDonald, I. R. (2020). Hydrocarbon migration pathway and methane budget for a Gulf of Mexico natural seep site: Green Canyon 600. *Earth and Planetary Science Letters, 545*, 116411. doi:10.1016/j.epsl.2020.116411

Jordan, S. F. A., Treude, T., Leifer, I., Janßen, R., Werner, J., Schulz-Vogt, H., & Schmale, O. (2020). Bubble-mediated transport of benthic microorganisms into the water column: Identification of methanotrophs and implication of seepage intensity on transport efficiency. *Scientific Reports, 10*(1), 4682. doi:10.1038/s41598-020-61446-9

Judd, A., & Hovland, M. (2007). *Seabed fluid flow: The impact on geology, biology and the marine environment*. Cambridge, UK: Cambridge University Press.

Kasaya, T., Mitsuzawa, K., Goto, T.-n., Iwase, R., Sayanagi, K., Araki, E., . . . Nagao, T. (2009). Trial of multidisciplinary observation at an expandable sub-marine cabled station "Off-Hatsushima Island Observatory" in Sagami Bay, Japan. *Sensors, 9*(11), 9241-9254. doi:10.3390/s91109241

Leifer, I. (2010). Characteristics and scaling of bubble plumes from marine hydrocarbon seepage in the Coal Oil Point seep field. *Journal Geophysical Research, 115*(C11), C11014. doi:10.1029/2009JC005844

Leifer, I. (2015). Seabed bubble flux estimation by calibrated video survey for a large blowout seep in the North Sea. *Journal of Marine and Petroleum Geology, 68B*, 743-752. doi:10.1016/j.marpetgeo.2015.08.032

Leifer, I. (2019). A synthesis review of emissions and fates for the Coal Oil Point marine hydrocarbon seep field and California marine seepage. *Geofluids, 2019*(4724587), 1-48. doi:10.1155/2019/4724587

Leifer, I., & Boles, J. (2005). Turbine tent measurements of marine hydrocarbon seeps on subhourly timescales. *Journal of Geophysical Research-Oceans, 110*(C1), C01006. doi:10.1029/2003jc002207

Leifer, I., Boles, J. R., Luyendyk, B. P., & Clark, J. F. (2004). Transient discharges from marine hydrocarbon seeps: Spatial and temporal variability. *Environmental Geology, 46*(8), 1038-1052. doi:10.1007/s00254-004-1091-3

Leifer, I., Chernykh, D., Shakhova, N., & Semiletov, I. (2017). Sonar gas flux estimation by bubble insonification: Application to methane bubble flux from seep areas in the outer Laptev Sea. *The Cryosphere, 11*(3), 1333-1350. doi:10.5194/tc-11-1333-2017

Leifer, I., & Clark, J. F. (2002). Modeling trace gases in hydrocarbon seep bubbles: Application to marine hydrocarbon seeps in the Santa Barbara Channel. *Geologiya I Geofizika, 47*(7), 572-579.

https://doi.org/10.5194/acp-2020-1234
Preprint. Discussion started: 6 July 2021

988 Leifer, I., Clark, J. F., & Chen, R. F. (2000). Modifications of the local environment by natural
989 marine hydrocarbon seeps. *Geophysical Research Letters, 27*(22), 3711-3714.
990 doi:10.1029/2000GL011619
991 Leifer, I., Jeuthe, H., Gjøsund, S. H., & Johansen, V. (2009). Engineered and natural marine
992 seep, bubble-driven buoyancy flows. *Journal of Physical Oceanography, 39*(12), 3071-
993 3090. doi:10.1175/2009JPO4135.1
994 Leifer, I., Kamerling, M., Luyendyk, B. P., & Wilson, D. (2010). Geologic control of natural
995 marine hydrocarbon seep emissions, Coal Oil Point seep field, California. *Geo-Marine*
996 *Letters, 30*(3-4), 331-338. doi:10.1007/s00367-010-0188-9
997 Leifer, I., Luyendyk, B. P., Boles, J., & Clark, J. F. (2006). Natural marine seepage blowout:
998 Contribution to atmospheric methane. *Global Biogeochemical Cycles, 20*(3), GB3008.
999 doi:10.1029/2005GB002668
1000 Leifer, I., & MacDonald, I. (2003). Dynamics of the gas flux from shallow gas hydrate deposits:
1001 interaction between oily hydrate bubbles and the oceanic environment. *Earth and*
1002 *Planetary Science Letters, 210*(3-4), 411-424. doi:10.1016/S0012-821X(03)00173-0
1003 Leifer, I., Melton, C., Fischer, M. L., Fladeland, M., Frash, J., Gore, W., . . . Yates, E. L. (2018).
1004 Atmospheric characterization through fused mobile airborne and surface in situ surveys:
1005 Methane emissions quantification from a producing oil field. *Atmospheric Measurement*
1006 *Techniques, 11*(3), 1689-1705. doi:10.5194/amt-11-1689-2018
1007 Leifer, I., Melton, C., Manish, G., & Leen, B. (2014). Mobile monitoring of methane leakage.
1008 *Gases and Instrumentation, July/August 2014*, 20-24.
1009 Leifer, I., Melton, C., Tratt, D. M., Buckland, K. N., Chang, C., Frash, J., . . . Yurganov, L.
1010 (2018). Validation of mobile in situ measurements of dairy husbandry emissions by
1011 fusion of airborne/surface remote sensing with seasonal context from the Chino Dairy
1012 Complex. *Environmental Pollution, 242*(Pt B), 2111-2134.
1013 doi:10.1016/j.envpol.2018.03.078
1014 Leifer, I., Melton, C., Tratt, D. M., Buckland, K. N., Clarisse, L., Coheur, P., . . . Yurganov, L.
1015 (2016). Remote sensing and in situ measurements of methane and ammonia emissions
1016 from a megacity dairy complex: Chino, CA. *Environmental Pollution, 221*, 37-51.
1017 doi:10.1016/j.envpol.2016.09.083
1018 Leifer, I., & Patro, R. (2002). The bubble mechanism for methane transport from the shallow
1019 seabed to the surface: A review and sensitivity study. *Continental Shelf Research, 22*(16),
1020 2409-2428. doi:10.1016/S0278-4343(02)00065-1
1021 Leifer, I., Solomon, E., Schneider v. Deimling, J., Coffin, R., Rehder, G., & Linke, P. (2015).
1022 The fate of bubbles in a large, intense bubble plume for stratified and unstratified water:
1023 Numerical simulations of 22/4b expedition field data. *Journal of Marine and Petroleum*
1024 *Geology, 68B*, 806-823. doi:10.1016/j.marpetgeo.2015.07.025
1025 Liss, P. S., & Duce, R. A. (2005). *The sea surface and global change*: Cambridge University
1026 Press.
1027 Liss, P. S., & Merlivat, L. (1986). Air-sea gas exchange rates: Introduction and synthesis. In P.
1028 Buat-Ménard (Ed.), *THe Role of Air-Sea Exchange in Geochemical Cycling* (Vol. 185).
1029 Dordrecht: Springer.
1030 Lu, R., Turco, R. P., & Jacobson, M. Z. (1997). An integrated air pollution modeling system for
1031 urban and regional scales: 1. Structure and performance. *Journal of Geophysical*
1032 *Research: Atmospheres, 102*(D5), 6063-6079. doi:10.1029/96jd03501

https://doi.org/10.5194/acp-2020-1234
Preprint. Discussion started: 6 July 2021

1033 Marinaro, G., Etiope, G., Bue, N. L., Favali, P., Papatheodorou, G., Christodoulou, D., . . . Rolin,
1034 J.-F. (2006). Monitoring of a methane-seeping pockmark by cabled benthic observatory
1035 (Patras Gulf, Greece). *Geo-Marine Letters, 26*(5), 297-302. doi:10.1007/s00367-006-
1036 0040-4
1037 Mazzini, A., Sciarra, A., Etiope, G., Sadavarte, P., Houweling, S., Pandey, S., & Husein, A.
1038 (2021). Relevant methane emission to the atmosphere from a geological gas
1039 manifestation. *Scientific Reports, 11*(1), 4138. doi:10.1038/s41598-021-83369-9
1040 Minor, S. A., Kellogg, K. S., Stanley, R. G., Gurrola, L. D., Keller, E. A., & Brandt, T. R.
1041 (Cartographer). (2009). Geologic Map of the Santa Barbara Coastal Plain Area, Santa
1042 Barbara County, California. Retrieved from https://pubs.usgs.gov/sim/3001/
1043 Münkel, C. (2007). Mixing height determination with lidar ceilometers - Results from Helsinki
1044 Testbed. *Meteorologische Zeitschrift, 16*, 451-459. doi:10.1127/0941-2948/2007/0221
1045 Muyakshin, S. I., & Sauter, E. (2010). The hydroacoustic method for the quantification of the gas
1046 flux from a submersed bubble plume. *Oceanology, 50*(6), 995-1001.
1047 doi:10.1134/S0001437010060202
1048 Nicewonger, M. R., Verhulst, K. R., Aydin, M., & Saltzman, E. S. (2016). Preindustrial
1049 atmospheric ethane levels inferred from polar ice cores: A constraint on the geologic
1050 sources of atmospheric ethane and methane. *Geophysical Research Letters, 43*(1), 214-
1051 221. doi:https://doi.org/10.1002/2015GL066854
1052 Nightingale, P. D., Malin, G., Law, C. S., Watson, A. J., Liss, P. S., Liddicoat, M. I., . . . Upstill-
1053 Goddard, R. C. (2000). In situ evaluation of air-sea gas exchange parameterizations using
1054 novel conservative and volatile tracers. *Global Biogeochemical Cycles, 14*(1), 373-387.
1055 doi:10.1029/1999GB900091
1056 Nisbet, E. G., Manning, M. R., Dlugokencky, E. J., Fisher, R. E., Lowry, D., Michel, S. E., . . .
1057 White, J. W. C. (2019). Very strong atmospheric methane growth in the 4 years 2014–
1058 2017: Implications for the Paris Agreement. *Global Biogeochemical Cycles, 33*(3), 318-
1059 342. doi:10.1029/2018GB006009
1060 Olson, D. J. (1983). *Surface and subsurface geology of the Santa Barbara Goleta Metropolitan*
1061 *area, Santa Barbara County, California.* (MS). Oregon State University, Retrieved from
1062 https://ir.library.oregonstate.edu/concern/graduate_thesis_or_dissertations/v692tb957?loc
1063 ale=it
1064 Padilla, A. M., Loranger, S., Kinnaman, F. S., Valentine, D. L., & Weber, T. C. (2019). Modern
1065 assessment of natural hydrocarbon gas flux at the Coal Oil Point seep field, Santa
1066 Barbara, California. *Journal of Geophysical Research: Oceans, 124*(4), 2472-2484.
1067 doi:10.1029/2018jc014573
1068 Peischl, J., Ryerson, T. B., Brioude, J., Aikin, K. C., Andrews, A. E., Atlas, E., . . . Parrish, D. D.
1069 (2013). Quantifying sources of methane using light alkanes in the Los Angeles basin,
1070 California. *Journal of Geophysical Research: Atmospheres, 118*(10), 4974-4990.
1071 doi:10.1002/jgrd.50413
1072 Pozzer, A., Pollmann, J., Taraborrelli, D., Jöckel, P., Helmig, D., Tans, P., . . . Lelieveld, J.
1073 (2010). Observed and simulated global distribution and budget of atmospheric
1074 C₂-C₅ alkanes. *Atmospheric Chemistray and Physics, 10*(9),
1075 4403-4422. doi:10.5194/acp-10-4403-2010
1076 Rahn, D. A., Parish, T. R., & Leon, D. (2017). Synthesis of observations from the Precision
1077 Atmospheric Marine Boundary Layer Experiment (PreAMBLE). *Monthly Weather*
1078 *Review, 145*(6), 2325-2342. doi:10.1175/mwr-d-16-0373.1

https://doi.org/10.5194/acp-2020-1234
Preprint. Discussion started: 6 July 2021

Reeburgh, W. S. (2007). Oceanic methane biogeochemistry. *Chemical Reviews, 107*(2), 486-513. doi:10.1021/cr050362v

Reeburgh, W. S., Ward, B. B., Whalen, S. C., Sandbeck, K. A., Kilpatrickt, K. A., & Kerkhof, L. J. (1991). Black Sea methane geochemistry. *Deep Sea Research Part A. Oceanographic Research Papers, 38*, S1189-S1210. doi:https://doi.org/10.1016/S0198-0149(10)80030-5

Rehder, G., Keir, R. S., Suess, E., & Rhein, M. (1999). Methane in the Northern Atlantic controlled by microbial oxidation and atmospheric history. *Geophysical Research Letters, 26*(5), 587-590. doi:10.1029/1999GL900049

Riedel, M., Scherwath, M., Römer, M., Veloso, M., Heesemann, M., & Spence, G. D. (2018). Distributed natural gas venting offshore along the Cascadia margin. *Nature Communications, 9*(1), 3264. doi:10.1038/s41467-018-05736-x

Römer, M., Hsu, C.-W., Loher, M., MacDonald, I. R., dos Santos Ferreira, C., Pape, T., . . . Sahling, H. (2019). Amount and fate of gas and oil discharged at 3400 m water depth from a natural seep site in the Southern Gulf of Mexico. *Frontiers in Marine Science, 6*(700). doi:10.3389/fmars.2019.00700

Römer, M., Riedel, M., Scherwath, M., Heesemann, M., & Spence, G. D. (2016). Tidally controlled gas bubble emissions: A comprehensive study using long-term monitoring data from the NEPTUNE cabled observatory offshore Vancouver Island. *Geochemistry, Geophysics, Geosystems, 17*(9), 3797-3814. doi:10.1002/2016GC006528

Römer, M., Sahling, H., Pape, T., Bohrmann, G., & Spieß, V. (2012). Quantification of gas bubble emissions from submarine hydrocarbon seeps at the Makran continental margin (offshore Pakistan). *Journal of Geophysical Research: Oceans, 117*(C10), C10015. doi:10.1029/2011jc007424

Römer, M., Wenau, S., Mau, S., Veloso, M., Greinert, J., Schlüter, M., & Bohrmann, G. (2017). Assessing marine gas emission activity and contribution to the atmospheric methane inventory: A multidisciplinary approach from the Dutch Dogger Bank seep area (North Sea). *Geochemistry, Geophysics, Geosystems, 18*(7), 2617-2633. doi:10.1002/2017gc006995

Saunois, M., Stavert, A. R., Poulter, B., Bousquet, P., Canadell, J. G., Jackson, R. B., . . . Zhuang, Q. (2020). The global methane budget 2000-2017. *Earth System Science Data, 12*(3), 1561-1623. doi:10.5194/essd-2019-128

Sauter, E. J., Muyakshin, S. I., Charlou, J.-L., Schlüter, M., Boetius, A., Jerosch, K., . . . Klages, M. (2006). Methane discharge from a deep-sea submarine mud volcano into the upper water column by gas hydrate-coated methane bubbles. *Earth and Planetary Science Letters, 243*(3-4), 354-365. doi:10.1016/j.epsl.2006.01.041

Scherwath, M., Thomsen, L., Riedel, M., Römer, M., Chatzievangelou, D., Schwendner, J., . . . Heesemann, M. (2019). Ocean observatories as a tool to advance gas hydrate research. *Earth and Space Science, 6*(12), 2644-2652. doi:10.1029/2019ea000762

Schmale, O., Beaubien, S. E., Rehder, G., Greinert, J., & Lonmbardi, S. (2010). Gas seepage in the Dnepr paleo-delta area (NW-Black Sea) and its regional impact on the water column methane cycle. *Journal of Marine Systems, 80*(1-2), 90-100. doi:10.1016/j.jmarsys.2009.10.003

Schmale, O., Greinert, J., & Rehder, G. (2005). Methane emission from high-intensity marine gas seeps in the Black Sea into the atmosphere. *Geophysical Research Letters, 32*(7), L07609. doi:10.1029/2004gl021138

https://doi.org/10.5194/acp-2020-1234
Preprint. Discussion started: 6 July 2021

Schmale, O., Leifer, I., Stolle, C., Schneider von Deimling, J., Krause, S., Kießlich, K., . . . Treude, T. (2015). Bubble transport mechanism: Indications for a gas bubble-mediated innoculation of benthic methanotrophs into the water column. *Continental Shelf Research, 103*, 70-78. doi:10.1016/j.csr.2015.04.022

Schneider von Deimling, J., Rehder, G., Greinert, J., McGinnis, D. F., Boetius, A., & Linke, P. (2011). Quantification of seep-related methane gas emissions at Tommeliten, North Sea. *Continental Shelf Research, 31*, 867-878. doi:10.1016/j.csr.2011.02.012

Schwietzke, S., Sherwood, O. A., Bruhwiler, L. M. P., Miller, J. B., Etiope, G., Dlugokencky, E. J., . . . Tans, P. P. (2016). Upward revision of global fossil fuel methane emissions based on isotope database. *Nature, 538*(7623), 88-91. doi:10.1038/nature19797

Shakhova, N., Semiletov, I., Leifer, I., Rekant, P., Salyuk, A., & Kosmach, D. (2010). Geochemical and geophysical evidence of methane release over the East Siberian Arctic Shelf. *Journal of Geophysical Research, 115*(C8), C08007. doi:10.1029/2009JC005602

Shakhova, N., Semiletov, I., Salyuk, A., Iossoupov, V., Kosmach, D., & Gustafsson, O. (2010). Extensive methane venting to the atmosphere from sediments of the East Siberian Arctic Shelf. *Science, 327*, 1246-1249. doi:10.1126/science.1182221

Shakhova, N., Semiletov Igor P., Leifer, I., Sergienko, V., Salyuk, A., Kosmach, D., . . . Gustafsson, O. (2013). Ebullition and storm-induced methane release from the East Siberian Arctic Shelf. *Nature Geoscience, 7*, 64-70. doi:10.1038/ngeo2007

Shindell, D. T., Faluvegi, G., Bell, N., & Schmidt, G. A. (2005). An emissions-based view of climate forcing by methane and tropospheric ozone. *Geophysical Research Letters, 32*, L04803. doi:doi:10.1029/2004GL021900

Simpson, I. J., Sulbaek Andersen, M. P., Meinardi, S., Bruhwiler, L., Blake, N. J., Helmig, D., . . . Blake, D. R. (2012). Long-term decline of global atmospheric ethane concentrations and implications for methane. *Nature, 488*(7412), 490-494. doi:10.1038/nature11342

Solomon, E., Kastner, M., MacDonald, I. R., & Leifer, I. (2009). Considerable methane fluxes to the atmosphere from hydrocarbon seeps in the Gulf of Mexico. *Nature Geoscience, 2*, 561-565. doi:10.1038/NGEO574

Thompson, D., Leifer, I., Bovensman, H., Eastwood, M., Fladeland, M., Frankenberg, C., . . . Thorpe, A. K. (2015). Real-time remote detection and measurement for airborne imaging spectroscopy: A case study with methane. *Atmospheric Measurement Techniques, 8*, 1-46. doi:10.5194/amtd-8-1-2015

Thornton, B. F., Prytherch, J., Andersson, K., Brooks, I. M., Salisbury, D., Tjernström, M., & Crill, P. M. (2020). Shipborne eddy covariance observations of methane fluxes constrain Arctic sea emissions. *Science Advances, 6*(5), eaay7934. doi:10.1126/sciadv.aay7934

Veloso-Alarcón, M. E., Jansson, P., De Batist, M., Minshull, T. A., Westbrook, G. K., Pälike, H., . . . Greinert, J. (2019). Variability of acoustically evidenced methane bubble emissions offshore Western Svalbard. *Geophysical Research Letters, 46*(15), 9072-9081. doi:10.1029/2019gl082750

Wanninkhof, R., Asher, W. E., Ho, D. T., Sweeney, C., & McGillis, W. R. (2009). Advances in quantifying air-sea gas exchange and environmental forcing. *Annual Review of Marine Science, 1*(1), 213-244. doi:10.1146/annurev.marine.010908.163742

Washburn, L., Johnson, C., Gotschalk, C. G., & Egland, E. T. (2001). A gas capture buoy for measuring bubbling gas flux in oceans and lakes. *Journal of Atmospheric and Oceanic Technology, 18*, 1411-1420. doi:10.1175/1520-0426

https://doi.org/10.5194/acp-2020-1234
Preprint. Discussion started: 6 July 2021

1169 Weber, D., Marquez, B. A., Taylor, C., Raya, P., Contreras, P., Howard, D., . . . Doezema, L. A.
1170 (2017). Macroseepage of methane and light alkanes at the La Brea tar pits in Los
1171 Angeles. *Journal of Atmospheric Chemistry, 74*(3), 339-356. doi:10.1007/s10874-016-
1172 9346-4
1173 Weber, T. C., Mayer, L., Jerram, K., Beaudoin, J., Rzhanov, Y., & Lovalvo, D. (2014). Acoustic
1174 estimates of methane gas flux from the seabed in a 6000 km2 region in the Northern Gulf
1175 of Mexico. *Geochemistry, Geophysics, Geosystems, 15*(5), 1911-1925.
1176 doi:10.1002/2014gc005271
1177 Wiggins, S. M., Leifer, I., Linke, P., & Hildebrand, J. A. (2015). Long-term acoustic monitoring
1178 at North Sea well site 22/4b. *Journal of Marine and Petroleum Geology, 68*, 776-788.
1179 doi:10.1016/j.marpetgeo.2015.02.011
1180 Wilson, D., Leifer, I., & Maillard, E. (2015). Megaplume bubble process visualization by 3D
1181 multibeam sonar mapping. *Journal of Marine and Petroleum Geology, 68B*, 753-765.
1182 doi:10.1016/j.marpetgeo.2015.07.007
1183 Zhao, D., Toba, Y., Suzuki, Y., & Komori, S. (2003). Effect of wind waves on air'sea gas
1184 exchange: Proposal of an overall CO2 transfer velocity formula as a function of breaking-
1185 wave parameter. *Tellus B: Chemical and Physical Meteorology, 55*(2), 478-487.
1186 doi:10.3402/tellusb.v55i2.16747
1187

https://doi.org/10.5194/acp-2020-1234
Preprint. Discussion started: 6 July 2021

Atmospheric Chemistry and Physics Discussions

Table of Nomenclature

$C_{ave}(\theta)$	Wind direction-resolved average concentration
C_{CH4}	Methane concentration
$C_{max}(\theta)$	Wind direction-resolved maximum concentration
$C_{med}(\theta)$	Wind direction-resolved median concentration
$C'_{Obs}(\theta)$	Wind direction-resolved WCS observed concentration
$C'_{Sim}(\theta)$	Wind direction-resolved WCS simulated concentration
$u_{ave}(\theta)$	Wind direction-resolved average u
$u_{ave}(\theta)$	Wind direction-resolved average u
$u_{max}(\theta)$	Wind direction-resolved maximum u
$u_{med}(\theta)$	Wind direction-resolved median u
C	Concentration
$C(t,\theta)$	Wind direction and time-resolved average concentration
$C'(i,j)$	Grid cell i, j plume concentration
$C'(\theta)$	Wind direction-resolved plume (anomaly) concentration
$C(\theta)$	Wind direction-resolved concentration
$E_A(i,j)$	Grid cell i, j atmospheric emissions
$E_A(\theta)$	Wind direction-resolved atmospheric emissions
E_B	Seabed (bottom) emissions
E_W	Emissions to the water column in the near field
i	Grid cell longitude index
j	Grid cell latitude index
$K(r,\theta)$	Wind direction and distance-resolved correction function to emissions
$K(\theta)$	Wind direction-resolved correction function to emissions
r	Distance from WCS to cell i, j
R^2	Correlation coefficient
t	Time
u	Wind speed
$u(\theta)$	Wind direction-resolved wind speed
$\delta\theta$	Model wind direction resolution
$\phi(C)$	Concentration probability distribution
$\phi(u)$	Wind probability distribution
$\phi(\theta,C)$	Wind direction and concentration-resolved probability distribution
$\phi(\theta,u)$	Wind direction and wind speed-resolved probability distribution
$\phi(\omega)$	Sonar return probability distribution
$\phi_n(\omega)$	Sonar return probability
$\phi_n(E_A)$	Atmospheric emissions probability
θ	Wind direction
ω	Sonar return
$\omega(i,j)$	Grid cell i,j sonar return
ψ	Wind veering
ζ	Relative inshore and offshore emissions

https://doi.org/10.5194/acp-2020-1234
Preprint. Discussion started: 6 July 2021

Atmospheric Chemistry and Physics Discussions

Table 1. Atmospheric plume composition and model atmospheric emissions.

Gas	Fraction (%)	Emissions (m^3 dy^{-1})	Emissions (Mg yr^{-1})
CH_4	88.5	73,900	19,300
C_2H_6	3.1	2,590	1270
C_3H_8	4.2	3,510	2520
C_4H_{10}	2.76	2,300	2180
C_5H_{12}	1.11	930	1090
C_6H_{14}	0.13	110	150
C_6H_6	$4.4x10^{-5}$	4.0	4.7
C_7H_{16}	0.04	33	55
C_7H_8	$1.0x10^{-5}$	1.0	1.3
NMHC	11.3	9470	7280
C_1-C_7*	85	83,400	26,600
CO_2	15	18,000	12,900

* C_1-C_7 = THC

https://doi.org/10.5194/acp-2020-1234
Preprint. Discussion started: 6 July 2021

Atmospheric Chemistry and Physics Discussions

1250

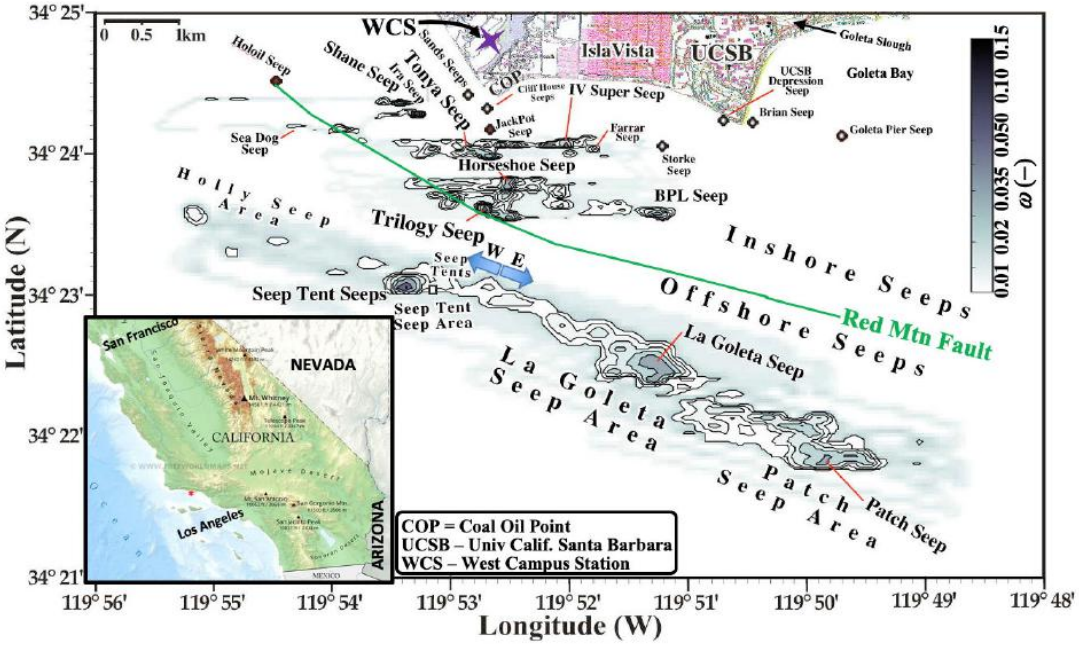

1251
1252 **Figure 1:** Sonar return, ω, map after Leifer et al. (2010). Purple star marks West Campus Station (WCS). Seep names are informal
1253 (**Table S3**), font size corresponds to strength. E-W arrow segregates east and west offshore seepage. Data keys on panels. Inset
1254 shows S. California, red dot marks COP seep field. California inset map from Freeworldmaps (2020).

1255

https://doi.org/10.5194/acp-2020-1234
Preprint. Discussion started: 6 July 2021

Atmospheric Chemistry and Physics Discussions

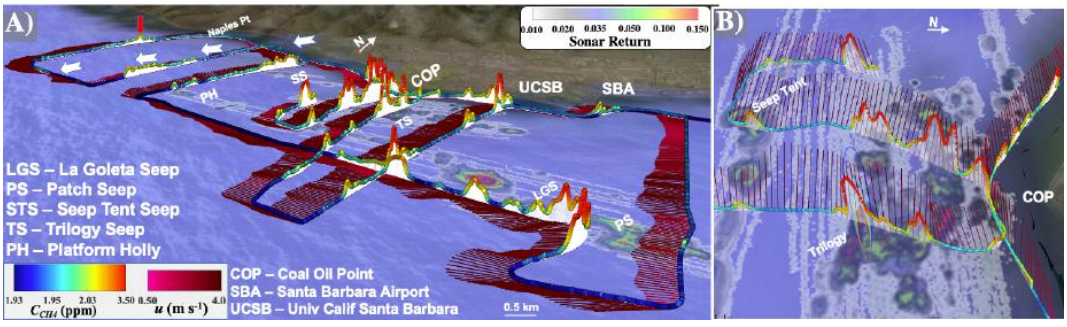

Figure 2: A) COP seep field methane, C_{CH4}, and winds, u, data for 28 May 2016. White arrows show canyon offshore flow. Red arrows show unmapped seepage to the west of the COP seep field. **B)** C_{CH4} and u showing Gaussian plume model for Trilogy Seep. Sonar return, ω, map in background. Data key and seep name key on panel. Displayed in Google Earth environment. **© Google Earth.** (See **Supp. Fig. S6** for overhead view).

https://doi.org/10.5194/acp-2020-1234
Preprint. Discussion started: 6 July 2021

Atmospheric Chemistry and Physics Discussions

1263

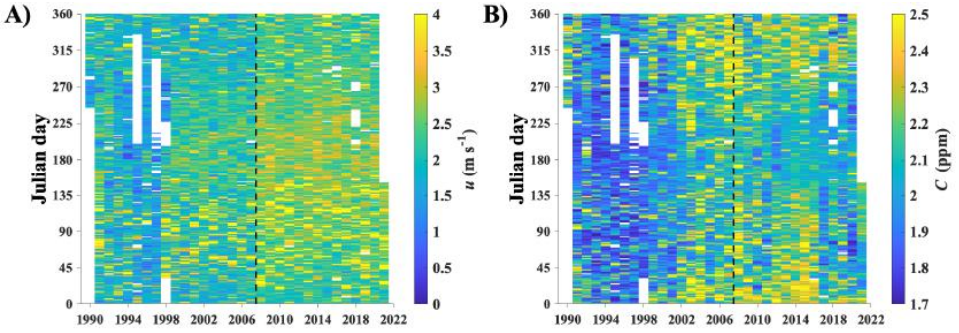

1264
1265 **Figure 3: A)** Daily mean wind speed, *u*, and **B)** total hydrocarbon concentration, *C*. Data key on figure. WCS upgrade on Jan 2008
1266 is shown by a dashed black line. **Supp. Fig. S4** shows raw dataset.

1267

https://doi.org/10.5194/acp-2020-1234
Preprint. Discussion started: 6 July 2021

Atmospheric Chemistry and Physics Discussions

1268

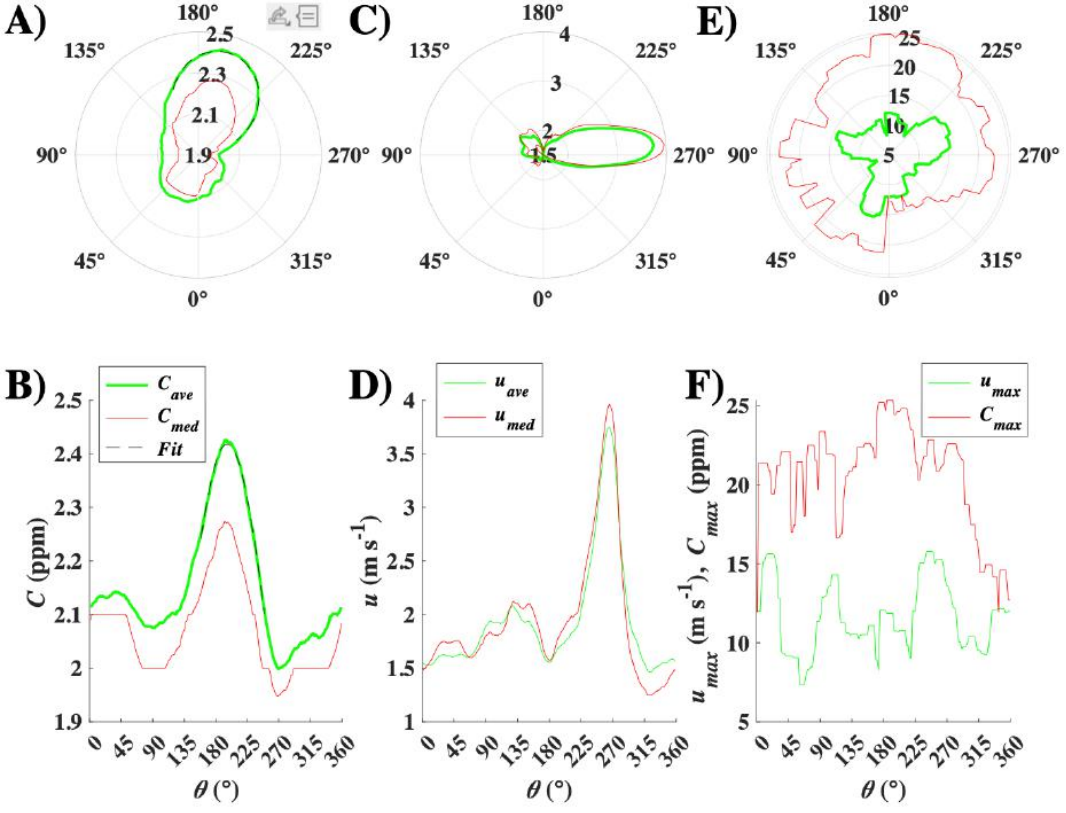

1269
1270 **Figure 4: A, B)** Concentration, C, versus wind-direction, θ, 1990-2021 for average, $\boldsymbol{C_{ave}(\theta)}$, and median, $\boldsymbol{C_{med}(\theta)}$, and fit to
1271 $\boldsymbol{C_{ave}(\theta)}$ for 155<θ<250°. Data key on panel B. **C, D)** Wind speed, u, average, $\boldsymbol{u_{ave}(\theta)}$, and median, $\boldsymbol{u_{med}(\theta)}$, Data key on panel
1272 D. and **E, F)** Maximum C, $\boldsymbol{C_{max}(\theta)}$, and wind speed, $\boldsymbol{u_{max}(\theta)}$. Data key on panel F. Polar plot oriented as at WCS facing the
1273 COP seep field.

1274

https://doi.org/10.5194/acp-2020-1234
Preprint. Discussion started: 6 July 2021

Atmospheric Chemistry and Physics Discussions

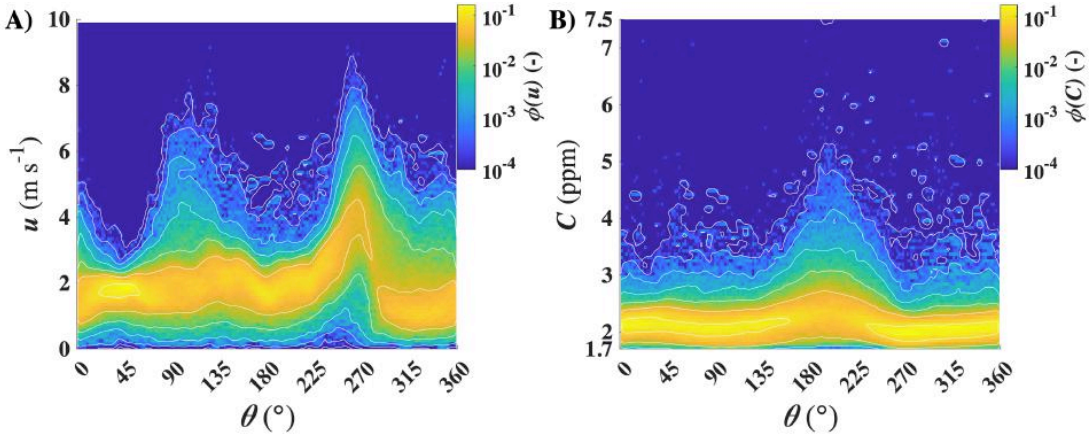

Figure 5: A) Wind-direction (θ) resolved wind-speed, u, probability distribution, $\phi(\theta,\boldsymbol{u})$ and **B)** Concentration probability distribution, $\phi(\theta, C)$, for 1990-2016. White dashed line shows edges of seep field. Data key on figure.

https://doi.org/10.5194/acp-2020-1234
Preprint. Discussion started: 6 July 2021

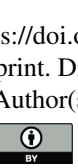

Atmospheric Chemistry and Physics Discussions

1279

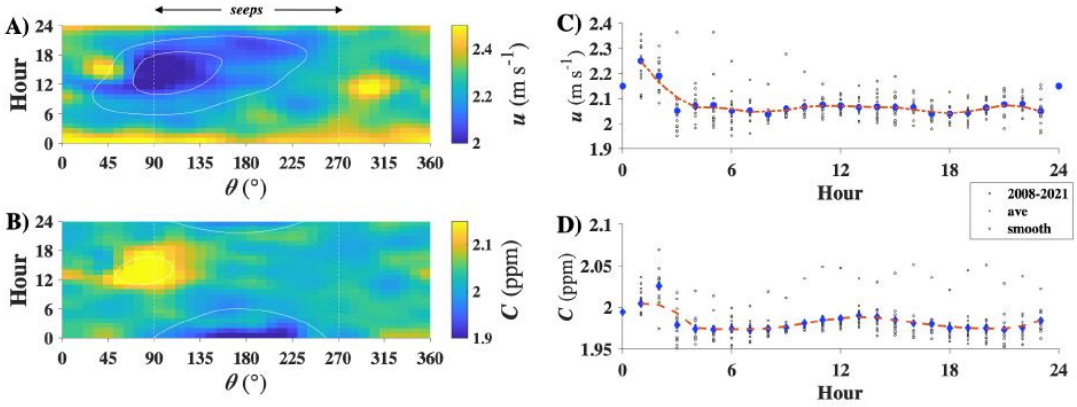

1280
1281 **Figure 6: A)** 2008-2021 averaged wind direction, *θ,* and hourly-resolved wind speed, *u*, and **B)** concentration, *C*. **C)** Seep-direction
1282 (90–270°), hourly-averaged wind speed, *u*, and **D)** concentration, *C*, averaged, individual years, and 3-year smoothed. Data key on
1283 figure. Midnight data missing due to daily calibration.

1284

https://doi.org/10.5194/acp-2020-1234
Preprint. Discussion started: 6 July 2021

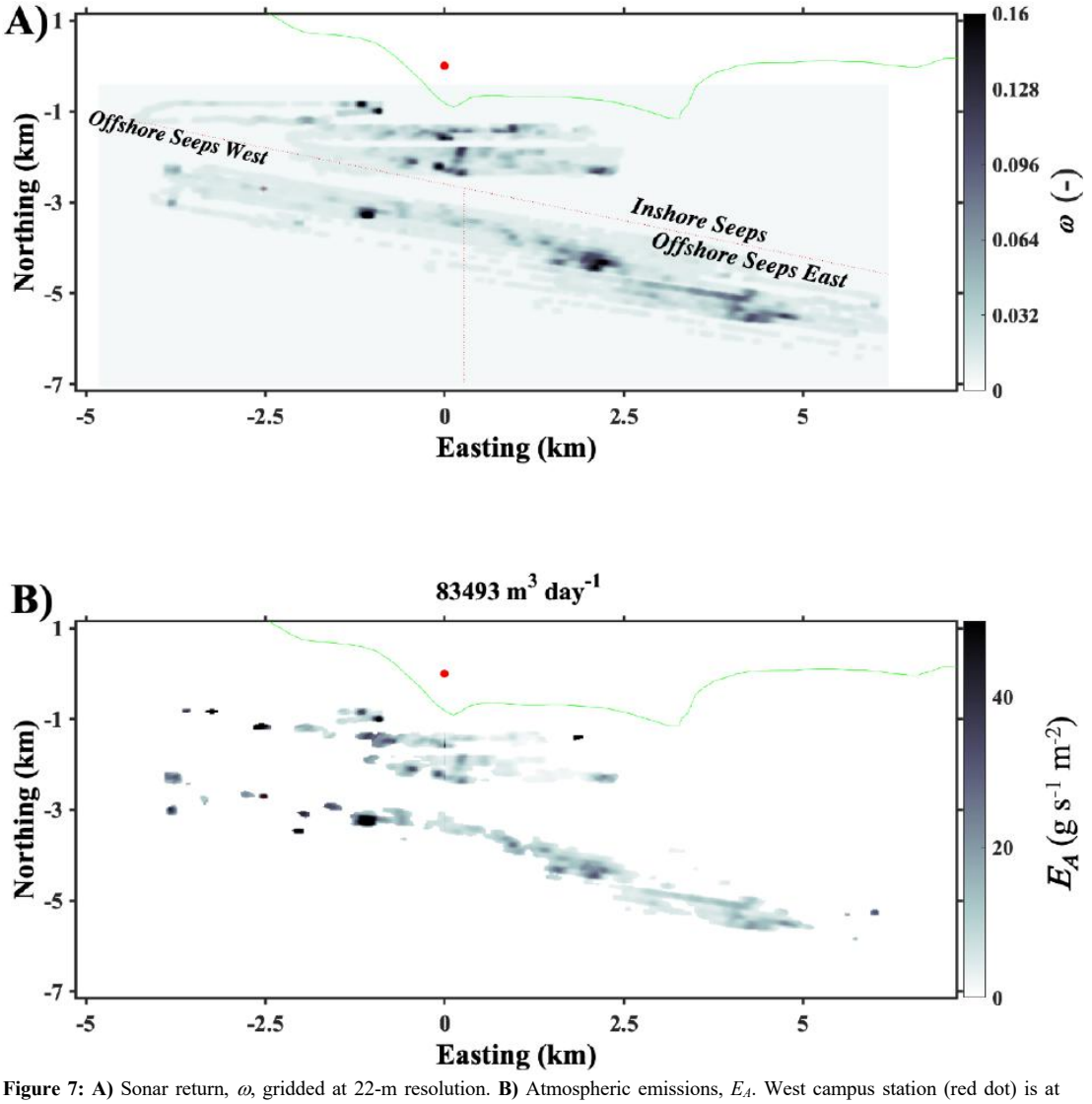

Figure 7: A) Sonar return, ω, gridded at 22-m resolution. **B)** Atmospheric emissions, E_A. West campus station (red dot) is at coordinate system origin. Green line is coast line.

https://doi.org/10.5194/acp-2020-1234
Preprint. Discussion started: 6 July 2021

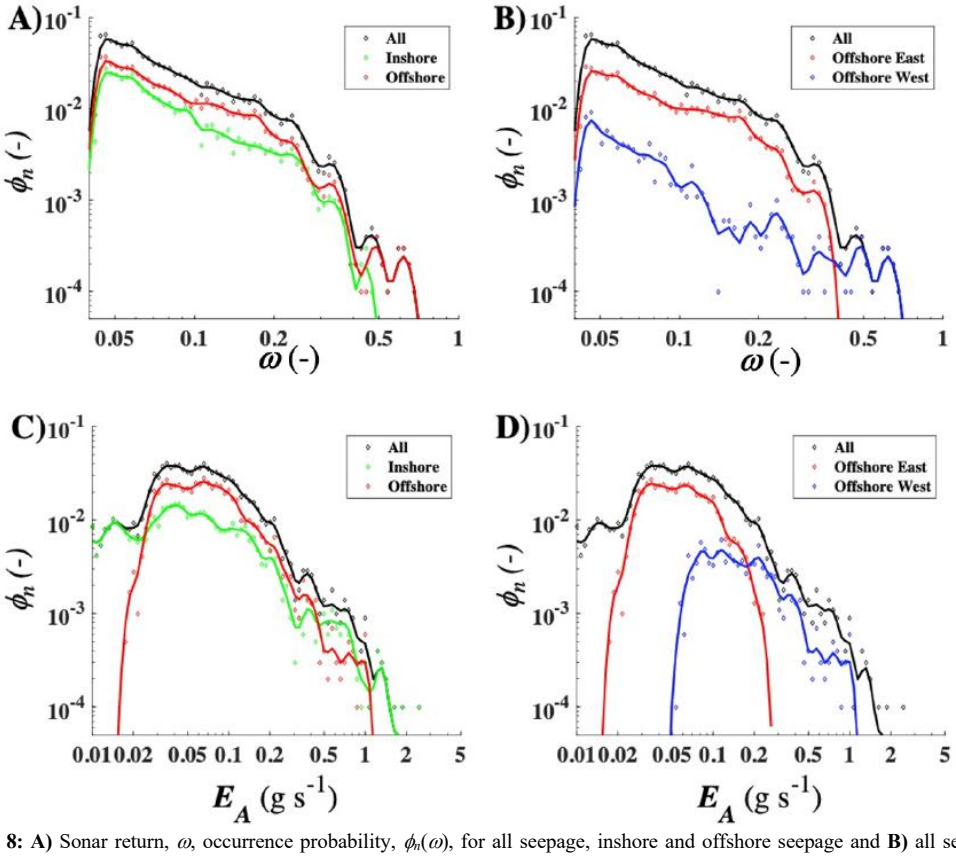

Figure 8: A) Sonar return, ω, occurrence probability, $\phi_n(\omega)$, for all seepage, inshore and offshore seepage and **B)** all seepage, offshore east seepage, and offshore west seepage. **C)** Atmospheric emission, E_A, occurrence probability, $\phi_n(E_A)$, for all seepage, inshore and offshore seepage and **D)** all seepage, offshore east seepage, and offshore west seepage. Data key on panels.

https://doi.org/10.5194/acp-2020-1234
Preprint. Discussion started: 6 July 2021

Atmospheric Chemistry and Physics Discussions

1294

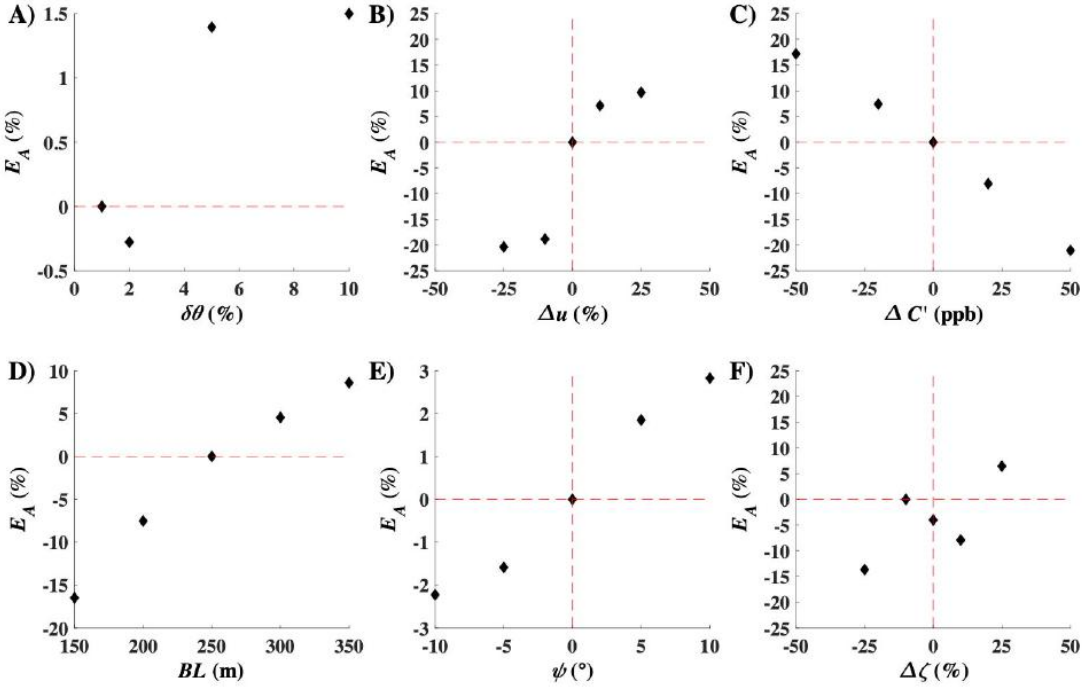

1295
1296 **Figure 9:** Emissions, E_A, sensitivity to uncertainty in **A)** model angular resolution, $\delta\theta$, **B)** wind speed variation, Δu, **C)**
1297 concentration anomaly variation, $\Delta C'$, **D)** boundary layer thickness, BL, **E)** wind veering, ψ, and **F)** inshore/offshore partition
1298 variation, $\Delta\zeta$. Note different units on different plots. See text for details.

1299

https://doi.org/10.5194/acp-2020-1234
Preprint. Discussion started: 6 July 2021

Atmospheric Chemistry and Physics Discussions

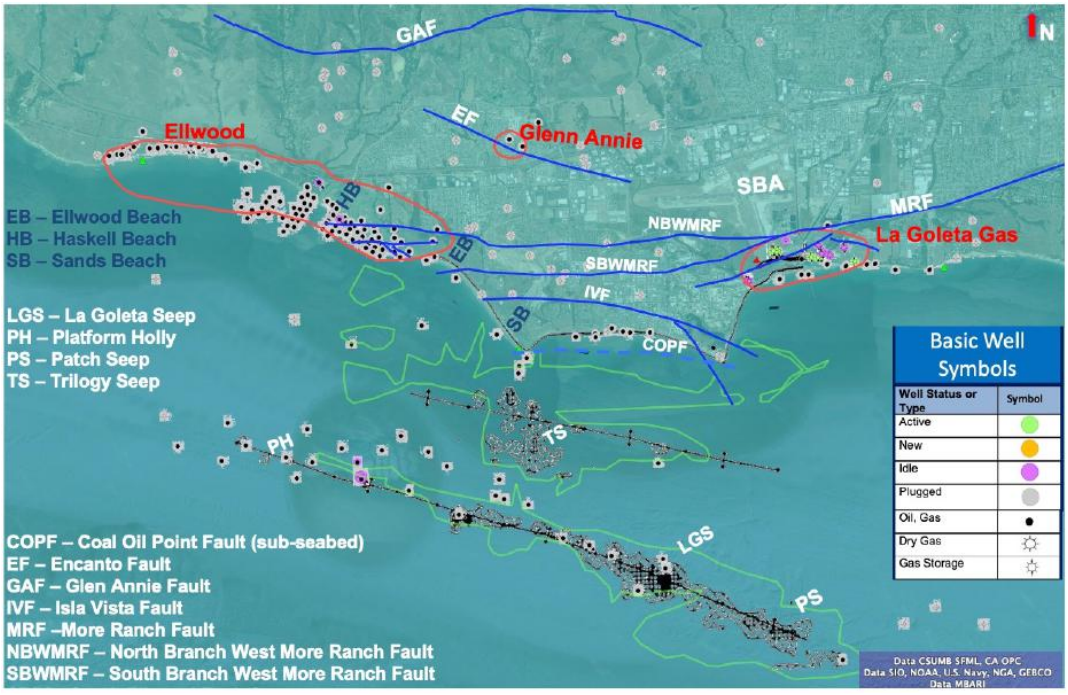

Figure 10: Map of the Goleta Plains oil and gas fields, wells, and the Coal Oil Point (COP) seep field. Grey hatch shows 1995 field extent, green outlines the 1940 field extent is from Leifer (2019). Field locations from Olson (1983). Well data from CDOGGR (2018). Faults from Minor et al. (2009). Seep names are informal. Data keys on panels. Shown in the © Google Earth environment.